SANDIA REPORT

SAND2013-8203
Unlimited Release
Printed October 2013

Dynamic temperature measurements with embedded optical sensors

Daniel H. Dolan, Christopher T. Seagle, and Tom Ao

Prepared by
Sandia National Laboratories
Albuquerque, New Mexico 87185 and Livermore, California 94550

Sandia National Laboratories is a multi-program laboratory managed and operated by Sandia Corporation, a wholly owned subsidiary of Lockheed Martin Corporation, for the U.S. Department of Energy's National Nuclear Security Administration under contract DE-AC04-94AL85000.

Approved for public release; further dissemination unlimited.

Sandia National Laboratories

Issued by Sandia National Laboratories, operated for the United States Department of Energy by Sandia Corporation.

NOTICE: This report was prepared as an account of work sponsored by an agency of the United States Government. Neither the United States Government, nor any agency thereof, nor any of their employees, nor any of their contractors, subcontractors, or their employees, make any warranty, express or implied, or assume any legal liability or responsibility for the accuracy, completeness, or usefulness of any information, apparatus, product, or process disclosed, or represent that its use would not infringe privately owned rights. Reference herein to any specific commercial product, process, or service by trade name, trademark, manufacturer, or otherwise, does not necessarily constitute or imply its endorsement, recommendation, or favoring by the United States Government, any agency thereof, or any of their contractors or subcontractors. The views and opinions expressed herein do not necessarily state or reflect those of the United States Government, any agency thereof, or any of their contractors.

Printed in the United States of America. This report has been reproduced directly from the best available copy.

Available to DOE and DOE contractors from
U.S. Department of Energy
Office of Scientific and Technical Information
P.O. Box 62
Oak Ridge, TN 37831

Telephone: (865) 576-8401
Facsimile: (865) 576-5728
E-Mail: reports@adonis.osti.gov
Online ordering: http://www.osti.gov/bridge

Available to the public from
U.S. Department of Commerce
National Technical Information Service
5285 Port Royal Rd
Springfield, VA 22161

Telephone: (800) 553-6847
Facsimile: (703) 605-6900
E-Mail: orders@ntis.fedworld.gov
Online ordering: http://www.ntis.gov/help/ordermethods.asp?loc=7-4-0#online

SAND2013-8203
Unlimited Release
Printed October 2013

Dynamic temperature measurements with embedded optical sensors

Daniel H. Dolan, Christopher T. Seagle, and Tom Ao
Sandia National Laboratories
P.O. Box 5800
Albuquerque, NM 87185-1189

Abstract

This report summarizes LDRD project number 151365, "Dynamic Temperature Measurements with Embedded Optical Sensors". The purpose of this project was to develop an optical sensor capable of detecting modest temperature states (<1000 K) with nanosecond time resolution, a recurring diagnostic need in dynamic compression experiments at the Sandia Z machine. Gold sensors were selected because the visible reflectance spectrum of gold varies strongly with temperature. A variety of static and dynamic measurements were performed to assess reflectance changes at different temperatures and pressures. Using a minimal optical model for gold, a plausible connection between static calibrations and dynamic measurements was found. With refinements to the model and diagnostic upgrades, embedded gold sensors seem capable of detecting minor (<50 K) temperature changes under dynamic compression.

Acknowledgments

Many individuals contributed to this project.

- Gold coatings for this project were prepared by Kathy Sobczak and Juan Romero in organization 1832.
- Room temperature and heated ellipsometry measurements were performed by Leslie Phinney in organization 1512.
- Static high pressure measurements, particularly the work at the Advanced Photon Source, were performed in collaboration with Nenad Velisavljevic (Los Alamos National Laboratory) and Jerry Stevens (National Security Technologies).
- Dynamic reflectance measurements were supported by Richard Hacking and Chase Smith (National Security Technologies).
- Impact experiment targets were built by Nicole Cofer and Dana Pariza (Raytheon)
- Additional experiment support, particularly development and testing of the heated impactor system, was provided by Andy Shay (organization 1342) and Aaron Bowers (Raytheon).
- Discussions with Michael Desjarlais, Martin French, and Luke Shulenburger contributed greatly to the development of the minimal gold model

This work was funded under LDRD project number 151365 and title "Dynamic Temperature Measurements with Embedded Optical Sensors".

Contents

1 Introduction **11**

1.1 Thermometry background 12

1.2 Reflectance thermometry 15

1.3 Project overview 18

2 Static gold measurements **19**

2.1 Previous work 19

2.2 Heated ellipsometry measurements 21

2.3 Diamond anvil cell measurements 23

3 Dynamic gold measurements **29**

3.1 Time-resolved reflectance measurements 30

3.2 Direct impact experiments on gold films 35

3.3 Known problems 41

4 Minimal gold model **45**

4.1 Model overview 46

4.2 Static temperature and pressure effects 49

4.3 Impact experiment comparison 55

5 Summary and future work **59**

References **61**

This page intentionally left blank.

List of Figures

1.1 Conceptual thermometry measurements 12

1.2 Limitations of optical pyrometry 13

1.3 Reflectance of gold at different temperatures 17

2.1 Previous measurements on heated gold 20

2.2 Ellipsometry measurements of unannealed gold 22

2.3 Ellipsometry measurements of annealed gold 24

2.4 DAC measurement setup at the APS 25

2.5 Reflectance measurements from the APS 26

2.6 Sandia DAC system 27

2.7 Room temperature DAC reflectance spectra 28

3.1 Conceptual gold sensor layout 29

3.2 SuperK light source evaluation 32

3.3 LDLS light source 33

3.4 Two-fiber reflectance probe 34

3.5 Dynamic reflectance system at DICE 34

3.6 Direct impact experiment layout 36

3.7 Standard DICE impact experiments 38

3.8 Heated projectile layout 39

3.9 Dynamic reflectance ratio images 40

3.10 Reflectance slices from experiment DG246 42

3.11 Consistency between gold coating batches 44

4.1 Previous interband models for gold 48
4.2 Minimal model applied to ambient gold samples 50
4.3 Gold parameter temperature trends 51
4.4 Reflectance ratio predictions at atmospheric pressure 53
4.5 Gold parameter pressure trends 54
4.6 Minimal model applied to direct impact measurement 56

List of Tables

1.1 Advantages and disadvantages of various thermometry techniques 15

3.1 Summary of impact experiments 37

4.1 Optical property relationships 46

4.2 Minimal model parameters for different sensor batches 50

This page intentionally left blank.

Chapter 1

Introduction

LDRD project #151365 was initiated in fiscal year 2011 and operated through fiscal year 2013. The goal of this project was to develop a high-speed temperature diagnostic for ramp wave compression experiments at the Sandia Z machine. In these experiments, samples are exposed to megabar pressure states over hundreds of nanoseconds.[1] Continuous, adiabatic compression causes sample temperature to rise, though substantially less than for shock wave compression to the same pressure. Actual temperature states in ramp or shock wave compression are largely unknown.

The importance of temperature in dynamic compression research is difficult to overstate. Thermodynamic equations of state,[2] such as the Helmholtz free energy $F(T, V)$, are intrinsically linked to temperature. While mechanical quantities (pressure, density, etc.) can be inferred from velocimetry measurements and conservation laws,[3] temperature cannot be determined in this way. This is unfortunate because temperature measurements more strongly constrain theoretical models than mechanical measurements, especially for off-Hugoniot states.[4] Furthermore, dynamic compression studies of phase transitions and chemical reactions are largely speculative without knowledge of the temperature states where these phenomena are observed. While temperature measurements are relatively simple under static conditions, they are extremely difficult in dynamic compression due to a host of diagnostic and physical limitations.

Three fundamental requirements guided the direction of this project.

1. The diagnostic must be sensitive to modest temperatures (< 1000 K).

2. The diagnostic must have fast time resolution (1–10 ns).

3. The diagnostic must be compatible with the harsh electromagnetic environment of Z.

As discussed in Section 1.1, standard temperature diagnostics fail one or more of these requirements. Section 1.2 describes an alternative approach based on reflectance thermometry, which can meet all three requirements. Section 1.3 describes the organization of project results in this report.

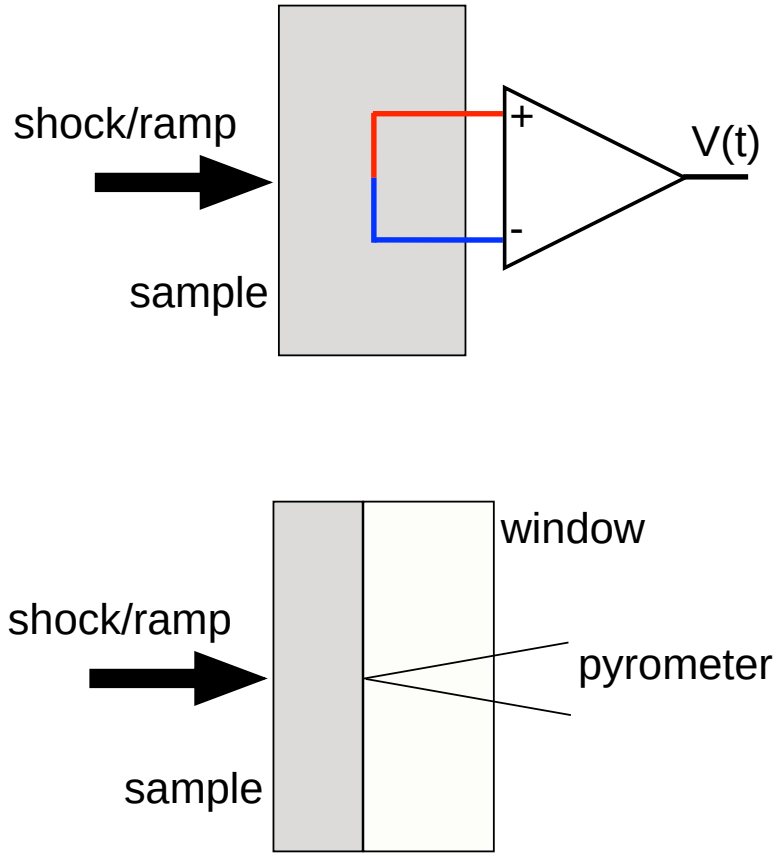

Figure 1.1. Conceptual layout of embedded thermocouple sensor (above) and optical pyrometry (below) measurements. The pyrometry example shown here assumes an opaque sample backed by a transparent window, which is needed to preserve a nonzero pressure state during the measurement.

1.1 Thermometry background

Suppose that a dynamic load (shock or ramp wave) is applied to a material of interest, causing a temperature change. Figure 1.1 illustrates two methods by which this temperature change could be measured. The embedded sensor technique is the most familiar and is based on properties of a standard material, such as the resistivity of copper. Properties of the standard change as the sample it is embedded within becomes warmer, so measurements on the standard provide information about the sample *assuming that the materials are in thermal equilibrium*. When the equilibrium condition is satisfied, thermometry measurements are effectively insensitive to properties of the sample (other than temperature). Electrical measurements—such as thermocouples[5] and thermistors[6]—are primary examples of sensor-based thermometry.

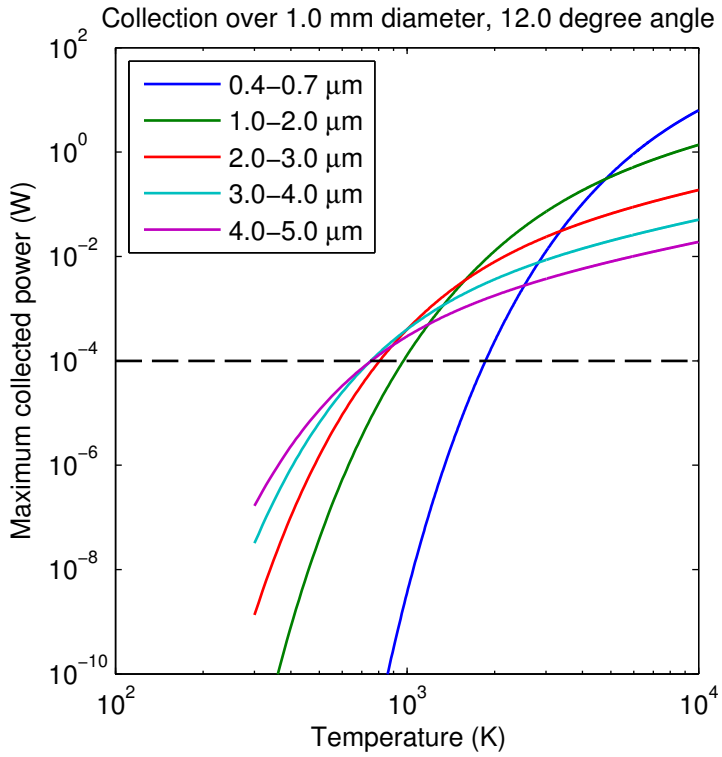

Figure 1.2. Practical limitations of optical pyrometry. Each curve indicates the maximum amount of power that can be collected in a particular spectral band, ignoring all losses. The dashed line indicates a generous estimate of the smallest detectable power in a measurement with nanosecond time resolution.

Optical pyrometry can also measure sample temperatures under dynamic compression. Unlike sensor-based techniques, pyrometry is intimately linked to sample temperature T. Plank's law:

$$\frac{dL}{d\lambda} = \epsilon(\lambda)\frac{2hc^2}{\lambda^5\left(e^{hc/\lambda kT} - 1\right)} \tag{1.1}$$

describes how the spectral radiance (power per unit area per unit solid angle per unit wavelength) emitted by the sample varies with wavelength λ. Measurements of this radiance in one or more spectral bands can be used to infer sample temperature *if sample emissivity* ϵ *is known*. Since optical measurements can be made very quickly and with minimal intrusion into the sample, dynamic pyrometry has been in use for some time.[7,8]

Plank's law is a strong function of temperature, which poses a problem for pyrometry measurements on short time scales. Figure 1.2 shows a plot of maximum power (integral of Equation 1.1) that could be collected in various spectral bands for a characteristic pyrometry measurement (sampling all light emitted in a 12° cone over a 1 mm diameter region). The

power collected in each band increases monotonically, with longer wavelengths bands initially collecting more power than shorter wavelength bands. Longer wavelength measurements are thus sensitive to lower temperatures, but there are practical limitations. Standard optical fiber will not pass wavelengths beyond 2 μm (2000 nm), and measurements beyond 5 μm (5000 nm) become impractical due to window opacity and limitations of mid-infrared fiber. For an unamplified[1] detection limit of 5 mV with a high-speed digitizer and a 50 V/W detector sensitivity (1 A/W into a 50 Ω load), the lowest detectable power is approximately 10^{-4} W. The curve in Figure 1.2 suggest that temperatures below 1000 K will largely fall below this threshold, especially when losses and sample emissivity (which is less than unity by definition) are considered. As a passive measurement, pyrometry signals are limited by light emission from the sample—when the sample isn't hot there is not much light to be collected.

Signal level is an issue in passive sensor measurements, such as embedded thermocouples, but active measurements are different. Since the output of an active measurement depends on an input signal, the output signal level can be controlled. In principle, a large input signal allows detection of small property changes in the sensor, allowing modest temperature changes to be detected. Embedded gauges, active and passive, are still subject to equilibration limits, which can be estimated from the thermal diffusivity κ.

$$\kappa \equiv \frac{\rho K}{c_p} = \frac{L^2}{T} \tag{1.2}$$

For a sensor thickness L, the characteristic equilibration time is $T = L^2/\kappa$, using the lowest diffusivity (sensor or sample). Noble metals (copper, silver, and gold) have thermal diffusivities of 10^{-4} m^2/s, suggesting equilibration on 10 ns time scales for 1000 nm sensor thicknesses; diffusivity is 10$\times$ lower for most metals and 100$\times$ lower for insulators, increasing the equilibration time respectively. Clearly there is a strong benefit to making ultrathin sensors for fast time resolution.[5,6] However, sensors that are too thin easily break during handling and/or dynamic loading.[9] Regardless of the sensor thickness or operating mode (active or passive), environment interference (EM pickup) is a persistent issue, especially in pulsed power environments.

Table 1.1 summarizes the advantages and disadvantages of embedded temperature sensors and optical pyrometry. Two additional techniques for measuring temperature—Raman and neutron resonance spectroscopy—are also included in this summary. Both methods have been successfully applied in dynamic compression experiments but are not in widespread use. Temperatures can be inferred from Raman spectra containing Stokes and anti-Stokes peaks; the amplitude ratio of these feature is related to a Boltzman factor.[4] Such measurements are only feasible in transparent samples with a reasonable Raman cross section, so many materials (such as metals) cannot be studied with Raman thermometry. Neutron resonance thermometry (NRS)[10] relies on minute differences in neutron absorption to detect temperature change in a tracer isotope embedded into the sample. NRS can probe temperatures

[1] Amplifying the detector signal does not improve the signal-noise ratio, so additional gain does not change this estimate. Low temperature pyrometry must also deal with background radiance, which may be comparable to the sample's radiance.

Table 1.1. Advantages and disadvantages of various thermometry techniques

Embedded electrical sensors	
Advantages	*Disadvantages*
Interpretation independent of sample properties	Sensor must equilibriate with sample
Adjustable signal levels (active techniques only)	Fragile connections
Low temperature sensitivity	
Optical pyrometry	
Advantages	*Disadvantages*
Direct sample measurement	Signal limited at low T
Robust, non-contact	Interpretation depends on sample
Raman spectroscopy	
Advantages	*Disadvantages*
Direct sample measurement	Cannot be used on opaque materials
Robust, non-contact	Extremely low signal levels
Neutron resonance spectroscopy	
Advantages	*Disadvantages*
Penetrates opaque samples	Requires intense neutron source

inside a metal sample, providing a unique method for determining bulk temperature. This method requires an intense source, such as the Los Alamos Neutron Science Experiment facility, and is thus restricted to very limited circumstances.

1.2 Reflectance thermometry

None of the methods described in Table 1.1 are suitable for high-speed temperature measurements during ramp wave compression. Embedded electrical sensors can detect the relevant temperature changes but face an unpleasant compromise: thick sensors (>0.001 mm) won't equilibrate with the sample quickly enough, but thin samples are easily broken before or during the experiment. Furthermore, electrical measurements are easily compromised in a pulsed power harsh environment. Optical pyrometry is robust to harsh environments and can be performed quickly if the sample is hot, but temperatures below 1000 K may not be detectable on nanosecond time scales. Pyrometry interpretation is also highly sample specific, so successful measurements (radiance and emissivity) for one material does not directly translate to another material.

Suppose that a standard material could be placed inside a dynamic compression experiment and probed optically. This approach avoids the interference and broken connections of embedded electrical gauges, yet preserves the use of a single standard that can be ported to a wide range of experiments. Requirements for this embedded optical sensor are given below.

- The sensor should be very thin (< 1000 nm) for fast equilibration with the sample.
- Sensor fabrication should be reasonably simple and reproducible.
- The sensor should be compatible with optical velocimetry, which is widely used in dynamic compression experiments.
- The optical measurement should be confined to the visible and near-infrared spectrum so that high-speed measurements are feasible.
- The optical measurement should be active rather than passive.

Combined with the proper standard material, reflectance thermometry can meet these requirements. Although this reflectance thermometry is commonly used in micro-scale measurements,[11–13] this project is the first application of the technique to dynamic compression experiments. The underlying idea is quite simple: heating a sample changes the optical properties of a material, altering its reflectance. This type of thermometry typically measures fractional reflectance changes at a single optical wavelength, often with small thermoreflectance coefficients (10^{-5}–10^{-4} 1/K).[14] Such minute changes can be detected via lock-in measurements, but would be not readily discernible in a single event measurement.

Gold is a particularly convenient material for thermoreflectance measurements at visible wavelengths. As shown in Figure 1.3, the reflectance of gold naturally transitions from about 40% at 400 nm to over 90% at 700 nm. Preferential absorption of blue light gives gold its characteristic color, and this color varies slightly with temperature. While the absolute change in reflectance at many wavelengths is imperceptible, the overall change of shape is significant.[15] Thermal effects are particular evident in the reflectance ratio:

$$Q(\lambda) \equiv \frac{R(\lambda, T)}{R(\lambda, T_0)} \tag{1.3}$$

where the reflectance at temperature T is normalized by the reflectance at a reference temperature T_0. By definition, $Q = 1$ for all wavelengths when gold is at the reference temperature. Upon heating, the ratio spectrum increases in the blue and decreases in the red, which is to say that the short wavelengths reflect slightly better and red wavelengths slightly worse. Ratio spectra at different temperatures appear to intersect at a wavelength (near 500 nm) sometimes called the "X-point", though the crossing is not identical at all temperatures.[16] The maximum and minimum excursions of Q about the X-point increase monotonically at roughly 2% per 100 K of temperature change.

The change of ratio spectrum shape with increasing temperature means that gold can be used an embedded sensors, similar to thermistors or thermocouples, with optical rather than electrical sampling. Such a sensor need only be a few hundred nanometers thick to achieve optical opacity and would thermally equilibrate faster than virtually any other standard because of gold's high thermal conductivity. Gold sensors can be deposited on samples and/or windows in a variety of ways (sputtering, electroplating, etc.), and would be sensitive to modest temperature changes (<100 K). Although its reflectance varies considerably in the

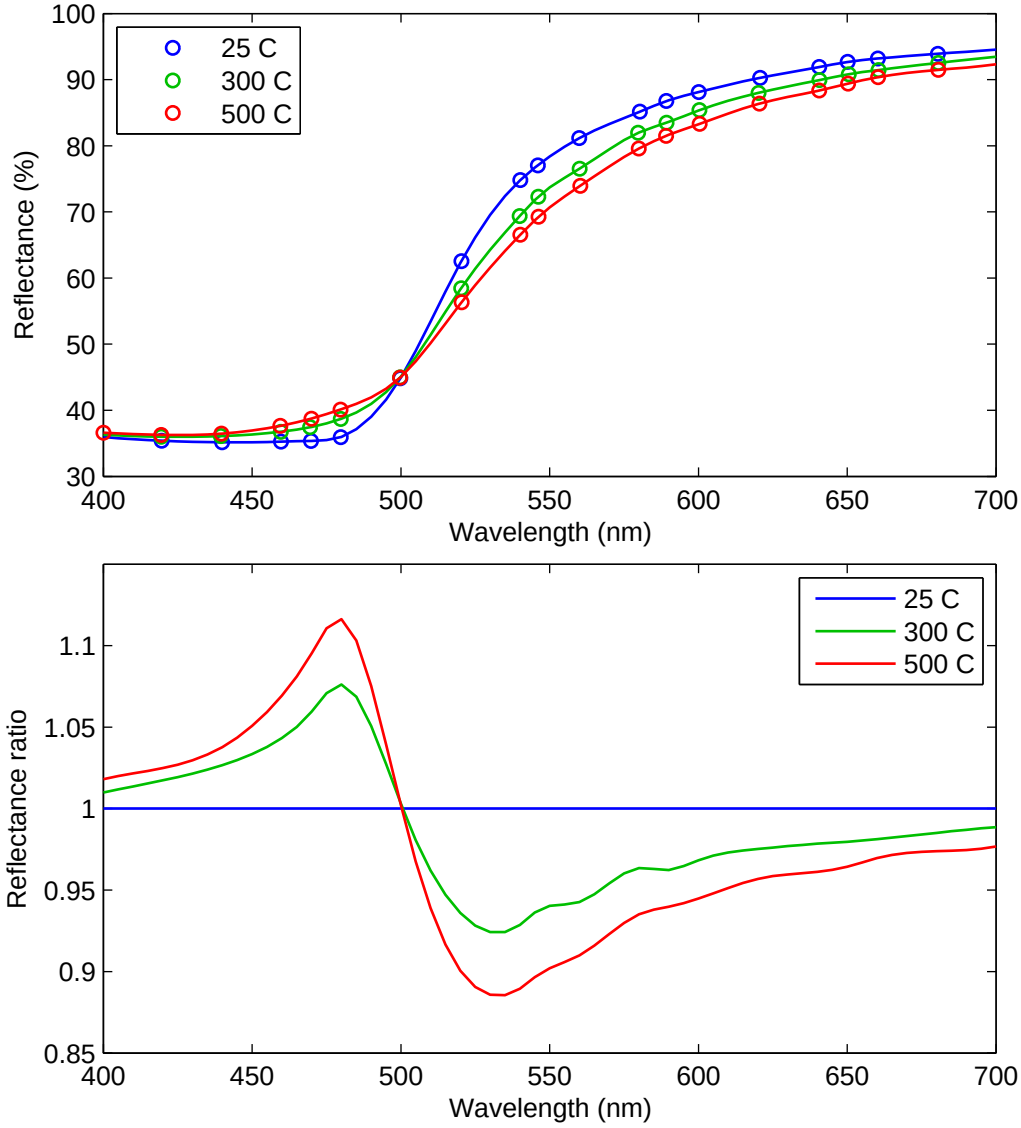

Figure 1.3. Reflectance and reflectance ratio of gold at different temperatures.[15]

visible spectrum, gold is a nearly perfect infrared reflector at 1550 nm, permitting simultaneous visible reflectance and infrared velocimetry[17] on the same sensor. As the ratio of outgoing to incoming optical power, reflectance signals can be controlled with the intensity of the a broad spectrum light source. Gold sensors can therefore meet all of the requirements listed above. Other materials, notably copper, could also be used in as sensor materials, but the chemical inertness of gold makes it the superior choice.

1.3 Project overview

Dynamic thermoreflectance measurements are more technically challenging than static approaches, but the methods are conceptually similar. The more fundamental challenge for dynamic gold sensors is calibration: given a measured reflectance ratio spectrum, can the sensor temperature be determined? If heating (which reduces material density) can alter the optical properties of gold, then presumably pressure (which increases density) also affects the reflectance spectrum. Decoupling these effects is crucial for gold to be a useful temperature sensor in dynamic compression research.

The results from this project are organized into three chapters, each focusing on a specific research area. Chapter 2 discusses static measurements of gold at different temperatures, both at ambient and elevated pressure. Chapter 3 deals with dynamic compression experiments on gold and the diagnostics/experiment capability developments made during the project. Chapter 4 presents a minimal optical model for gold needed to analyze static and dynamic measurements. A project summary and suggestions for future work is given in Chapter 5.

Chapter 2

Static gold measurements

This chapter discusses optical measurements on gold at fixed temperature and fixed pressure. These measurements provide a survey of gold's response to different thermodynamic states for sensor calibration. Calibration proved to be more complicated than anticipated at the outset of this project, and important details of this process are postponed until Chapter 4. This chapter focuses on the experimental results as they were obtained, emphasizing practical challenges encountered.

2.1 Previous work

Before delving into the work performed in this project, it is useful to consider previous optical measurements on gold. Many studies have been dedicated to the optical properties of gold at room temperature,[18–25] but heated[15,26–29] and cooled[30] measurements have also been reported. Figure 2.1 shows the heated reflectance measurements along with calculated ratio spectra. In all cases, the ratio of a higher temperature reflectance measurement to a lower temperature measurement shows the same general trend: increased reflectance in the blue and decreased reflectance in the red. This trend persists up to the melting point, indicating that gold sensors can be used to at least 1000° C at ambient pressure and perhaps higher with the application of pressure (which suppresses the melting transition[31]). Melting intensifies the increasing-blue/decreasing-red trend,[29] suggesting that density is strongly linked to the observed spectral changes.

Careful inspection of data from different sources indicates that the optical constants of gold are not truly constant, but rather vary with sample preparation. For example, the structure and optical properties of vapor-deposited gold vary dramatically with substrate temperature.[32] Aspnes[33] explored a range of gold preparations and found that that the measured differences could be attributed to sample porosity and grain size. Micro-structural variations can also be induced by heating films after deposition. Given sufficient time, grain boundaries can migrate at elevated temperature as observed directly by Rost.[34] These structural changes alter the optical properties of gold[35] in an irreversible manner, which means that changes observed in reflectance ratio spectrum may be a combination of current and previous temperature states.

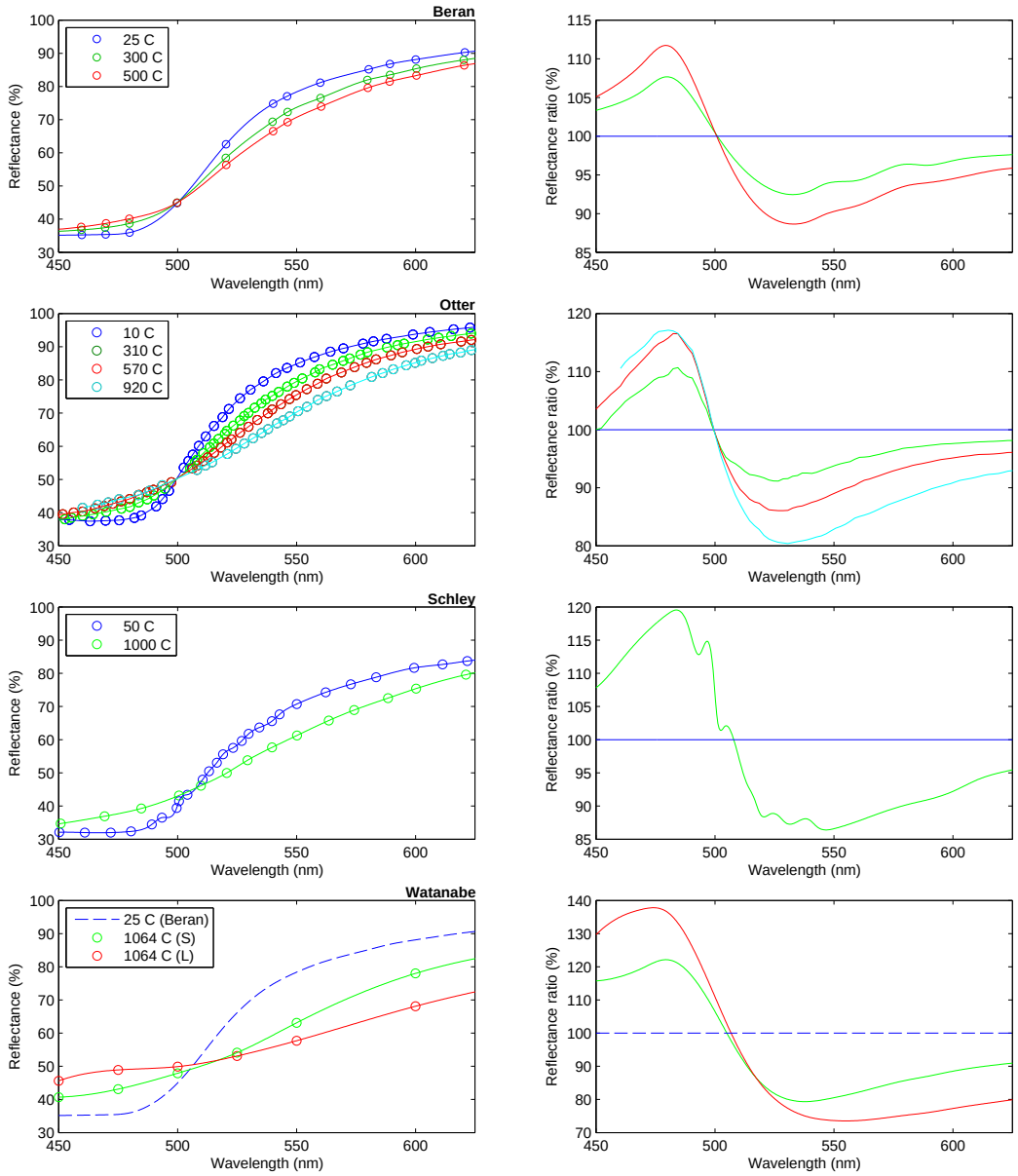

Figure 2.1. Previous optical measurements on gold a different temperatures. Ratio spectra from Beran,[15] Otter,[28] and Schley[27] are calculated with respect to the lowest temperature reported by each source. Watanabe[29] reported reflectance for solid (S) and liquid (L) gold at the melt point only, so these curves are normalized with Beran's 25° C data.

Since preparation and thermal history of a gold sample affects its optical properties, there is a risk that embedded sensor measurements may not be entirely reproducible. Several precautions can be taken to mitigate this risk.

- Gold sensors should be characterized as prepared rather than relying on literature results,[25] drawing at least one sample per batch for analysis.
- In static applications, gold sensors should be annealed at the conditions more extreme than expected in actual use. Holding the sensor at an elevated temperature for a long time allows the material to irreversibly stabilize; returning the sensor to room temperature should not cause the microstructure to revert to the original configuration.

Annealing at high temperature/pressure evolves over minute to hour time scales. Short-lived experiments—plate impact, pulsed power, etc.—occur on much shorter time scales, so it is unlikely that annealing plays any significant role in dynamic compression applications.

2.2 Heated ellipsometry measurements

Ambient pressure characterization of gold at elevated temperatures was performed at Sandia with a spectroscopic ellipsometer from J.A. Woollam Company. This ellipsometer performs multi-angle measurements at room temperature over the ultraviolet, visible, and near-infrared spectrum. When heated stages are installed, the ellipsometer is confined to a single angle but the spectral range is maintained. The original heating stage for this system could bring samples to temperatures as high as 300° C; a second stage was later purchased to support measurements as high as 600° C. In all heated ellipsometry scans, samples were allowed to stabilize for at least thirty minutes before associating data with the stage temperature.

Figure 2.2 shows the reflectance obtained from gold deposited on a sapphire window (similar to the sensors described in the next chapter) with no explicit heat treatment. To aid comparisons with previous work, the complex refractive index measured by the ellipsometer has been converted to reflectance ratio as described in Table 4.1 (page 46). During the first thermal cycle (25→75→150→275° C), the reflectance ratio spectra increases in the blue and decreases the red (with fixed reflectance near 500 nm) as expected. However, returning the sample to room temperature does not restore the reflectance to its original state. Instead, the trend normally observed in heating appears somewhat inverted, which could be naively interpreted as a temperature below the reference state. This hysteresis is caused by unintentional annealing—measuring the film's properties at elevated temperature for extended periods of time alters these properties.

While the lower temperature measurements differ between cycles, the highest temperature measurements in Figure 2.2 are extremely similar. This suggests that microstructure changes from the first cycle persist into the second cycle, with no further modifications at the

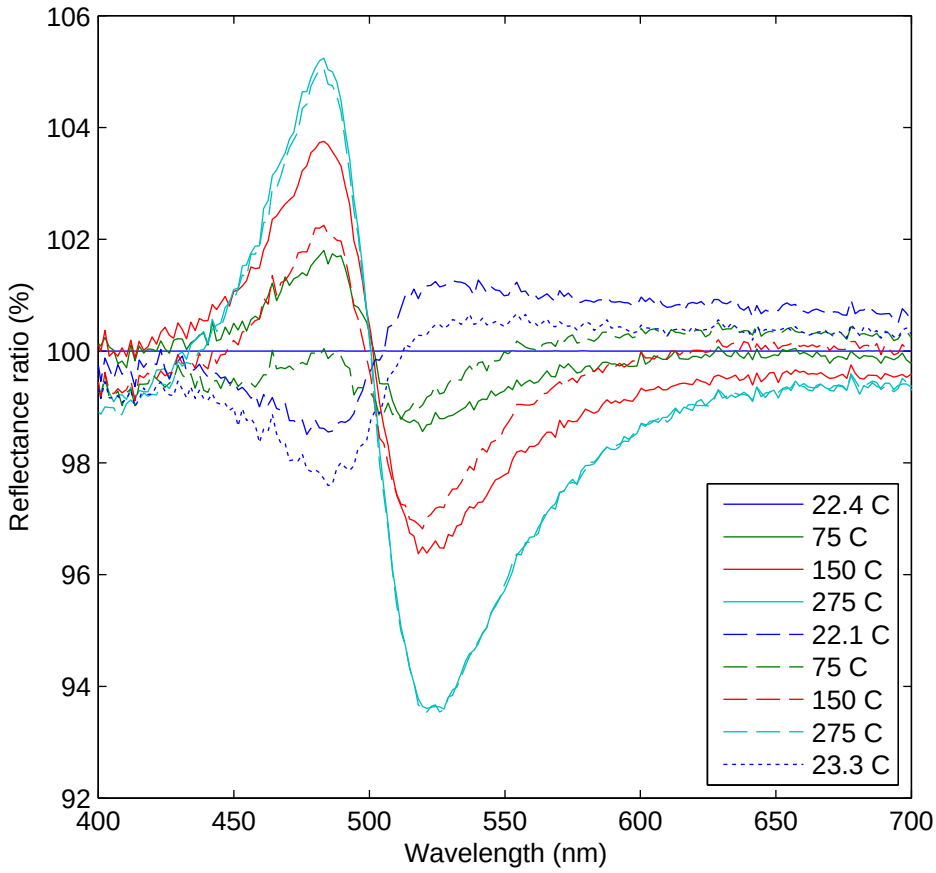

Figure 2.2. Reflectance spectra of unannealed gold through two cycles between room temperature and 275° C. Solid lines indicate the first heating cycle, dashed lines the second cycle. The dotted line is an ambient spectrum obtained after the two cycles.

temperature. To minimize this effect, subsequent ellipsometry scans were performed on an intentionally annealed sample. The sample was placed in a sealed oven, pumped to a rough vacuum and backfilled with nitrogen. The oven was heated to 250° C and held for at least four hours, after which time the oven was allowed to slowly cool back to room temperature (3–4 hours).

Figure 2.3 shows two heated ellipsometry runs on an annealed gold film. In the first run, the maximum temperature was 275° C, slightly higher than the 250° C annealing temperature. Unlike the unannealed scan, measurements of the annealed sample are highly reproducible at a given temperature; hysteresis is significantly less than 1% and there are no artifacts that could be confused with cooling. The second ellipsometry run was allowed to exceed the annealing temperature, resulting in noticeable hysteresis when the sample returned to room temperature.

These results indicate that precise characterization of gold in static measurements is highly dependent on thermodynamic history. Without appropriate annealing, reflectance changes observed in a gold sample are not purely a function of the current temperature (or pressure). This could be disastrous in static applications, so it is critical that sensors be consistently processed before calibration and installation.

2.3 Diamond anvil cell measurements

Reflectance measurements in the diamond anvil cell (DAC) were used to study the role of pressure in the reflectance of gold. This work utilized commercial DACs (EasyLab Helios) with a gas-driven membrane and resistive heating, capable of reaching 50 GPa pressures and 1000° C temperatures. Attempts to coat gold directly onto the diamond anvil were entirely unsuccessful, so it gold foils were used instead.

The first DAC campaigns on gold reflectance were performed with the Advanced Photon Source (APS) at Argonne National Laboratory (Figure 2.4). In these campaigns, gold foils were loaded into an indented Inconel gasket with platinum powder.[1] Monochromatic x-rays (30 keV) passing though the DAC provided measurements of platinum density, from which interior pressure was determined. Off-normal reflectance measurements of the gold pressed against one diamond face were obtained at different temperatures and pressures. Figure 2.5 shows one set of reflectance ratio spectra obtained at APS. Closing the DAC creates 1–2 GPa sample pressures at room temperature, and the first measurement taken under these conditions served as the reference state. The sample was heated to the desired temperature (300° C, in this case), causing the pressure increase as well. Isothermal compression was then performed, with ratio spectra collected along compression to 20 GPa, release to 5 GPa, and recompression to 18 GPa.

[1] A possible complication with this configuration is the formation of gold-platinum allows at high pressure/temperature[36]

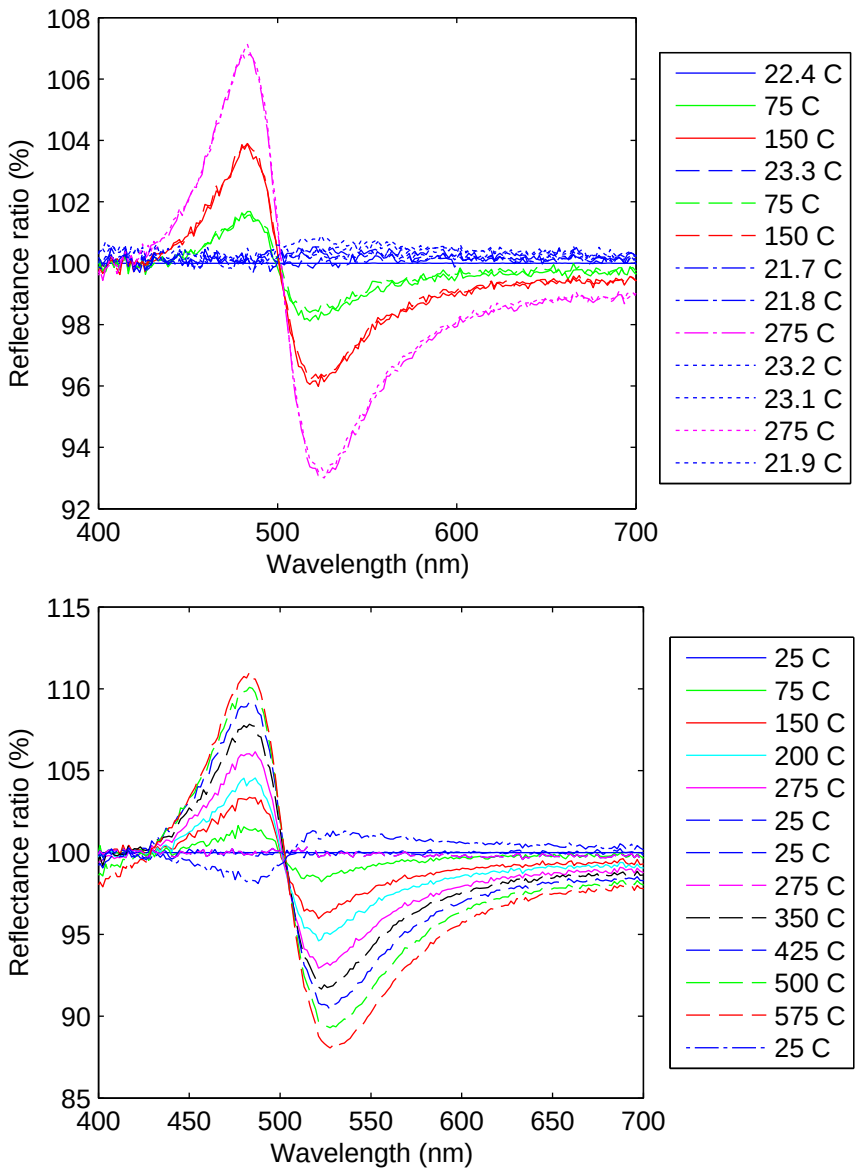

Figure 2.3. Ellipsometry measurements of annealed gold (250° C). Each heating cycle is represented by a common line style (solid, dashed, etc.).

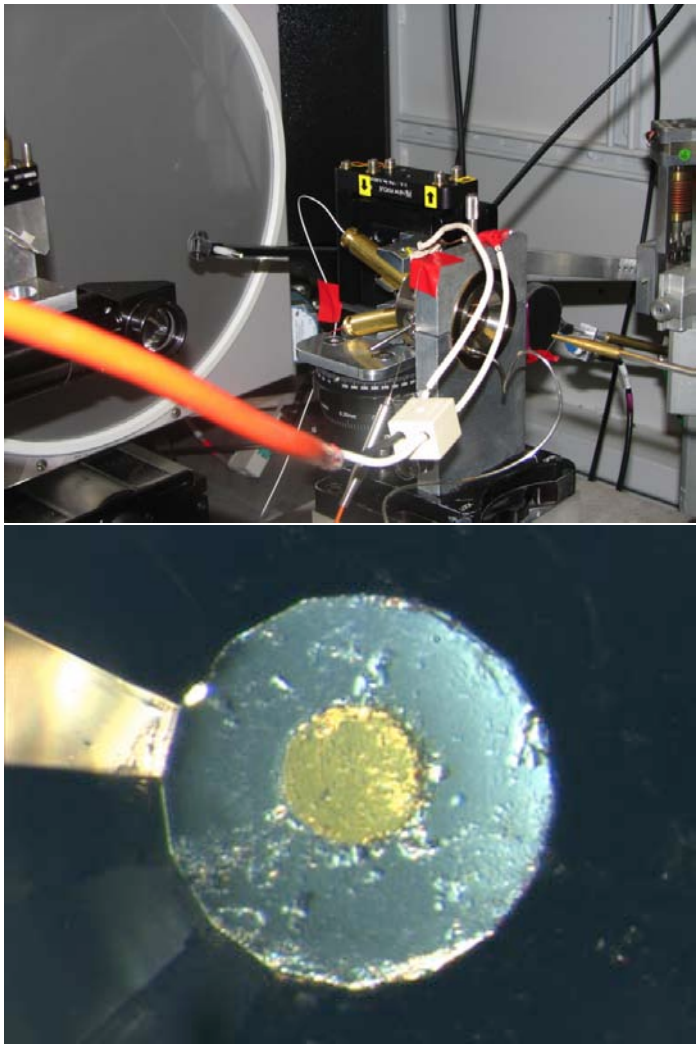

Figure 2.4. DAC measurement setup at the APS (above) The heated DAC is illuminated with hard x-rays emerging from the small aperture on the right. Diffraction from the platinum powder and gold foil are recorded on the large circular image plate on the left. The brass tubes positioned at $\pm 45°$ to the beam axes are for visible refection spectroscopy. (below) Inside the DAC, the gold foil rests inside a gasket placed on the diamond culet. The sample is nominally 0.10 mm in diameter.

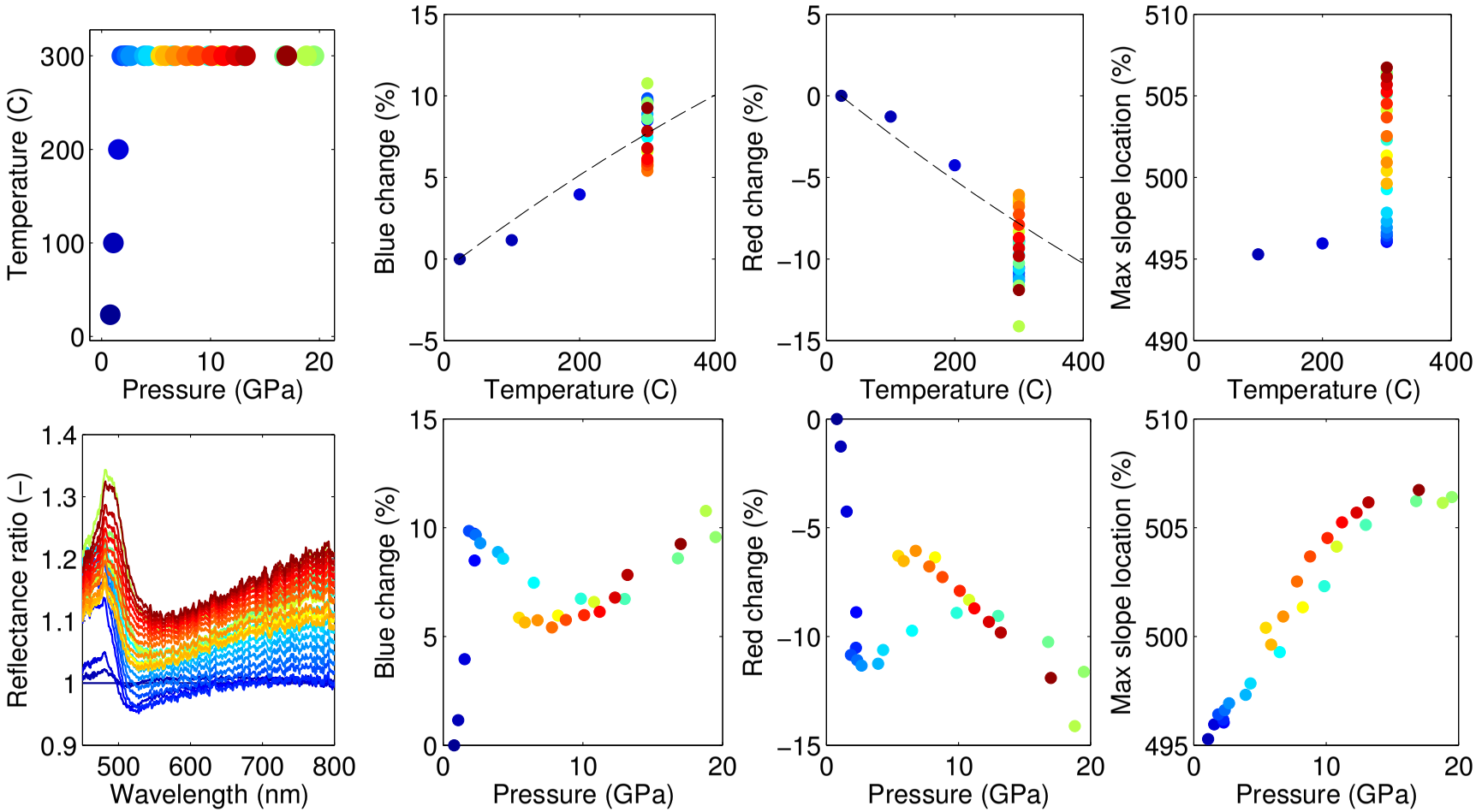

Figure 2.5. Static reflectance measurements obtained at the APS

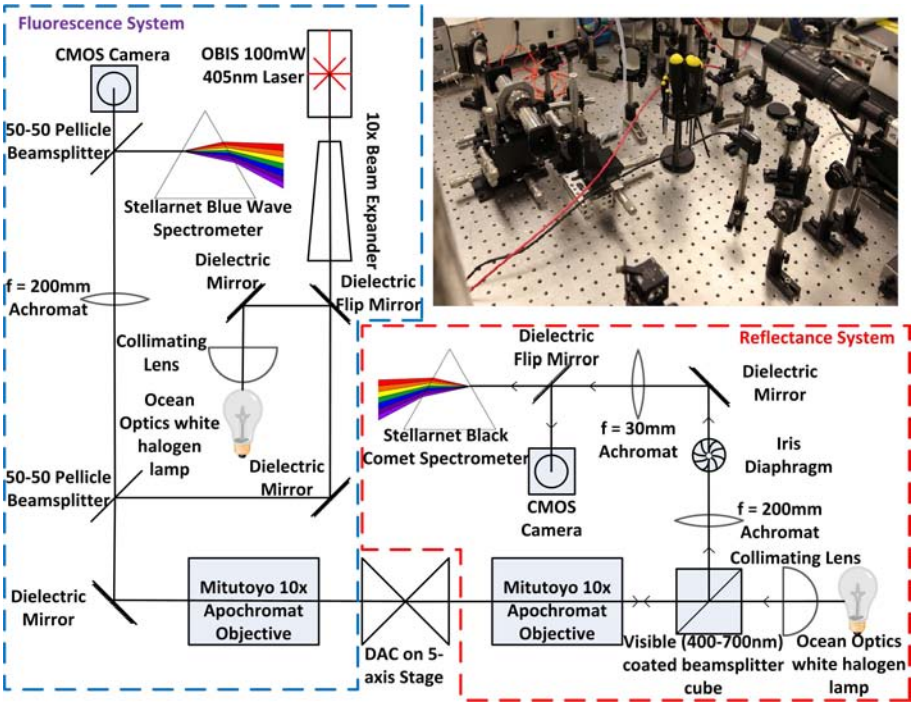

Figure 2.6. Sandia's diamond anvil cell system

As a conceptual aid, reflectance ratio spectra were reduced to three descriptive parameters. The wavelength of steepest ratio change was determined from a smoothed numerical derivative. The largest and smallest reflectance ratio values relative to this point ("blue" and "red" change, respectively) were then determined. The blue change was expected to become more positive and the red change more negative with temperature, and this trend was observed during the initial heating phase. Applying pressure initially had the opposite effect, driving the blue and red changes towards zero for pressures up to 10 GPa, after which the changes move away from zero. Releasing the pressure back to about 5 GPa partially reverses these variations, but upon recompression the changes do not retrace the first compression (especially on the red side). The position of maximum slope was much more reproducible, suggesting that this parameter is primarily a function of pressure with little hysteresis.

Three experimental campaigns were attempted at APS during this project. Qualitatively, results similar to Figure 2.5 were obtained in different isothermal compressions. Unfortunately, a number of technical problems prevented this data from be more quantitatively useful. In a number of experiments, the gasket moved during release and recompression, contaminating the reflectance measurement with a combination of gold and Inconel. Even when experiments were confined to pure compression, minor changes in the sample position during compression could move the reflectance spot off the center of the gold sample. Given the access restrictions of working with an x-ray source, it was difficult to detect and correct optical alignment issues as they occurred. Linearity in the reflectance measurements was also found to be an issue.

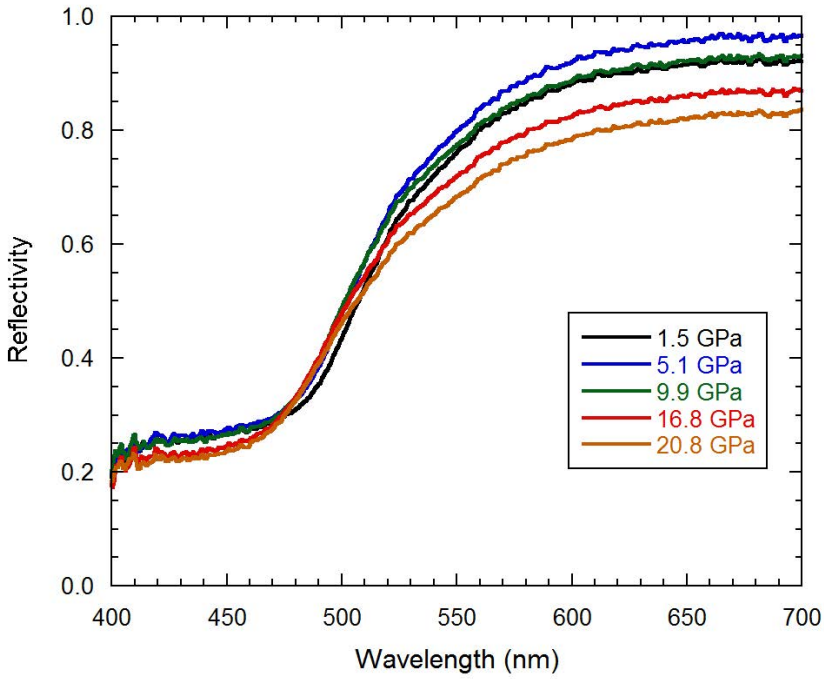

Figure 2.7. Room temperature DAC reflectance spectra

A new DAC reflectance system was developed at Sandia to help address these problems. Reference 37 provides a detailed description of this system, so only a brief summary is given here. Gold foils were compressed in the same heated DAC model as the APS experiments, but without an x-ray source. Pressure was determined by ruby fluorescence through one of the diamond anvils, and on-axis reflectance was measured from the other side (on axis). Rigorous testing of the optical spectrometer (Black Comet) indicated that the measurements were truly linear in optical power. An imaging capability was included with the system to verify optical alignment when the sample was heated and compressed. Measurements were periodically recalibrated against an absolute standard, yielding absolute reflectance rather than reflectance ratio spectra.

Figure 2.7 shows measurements of gold reflectance at room temperature for several pressures. The results suggest that pressure shifts the steepest part of the reflectance curve to shorter wavelengths, while also broadening the transition from high to low reflectance. This data, along with isothermal measurements at 160° C and 230° C, is analyzed in greater detail in Chapter 4.

Chapter 3

Dynamic gold measurements

Dynamic measurements are the true test for gold sensors in shock and ramp wave compression experiments. While static measurements provide insights about gold at elevated temperatures and pressures, dynamic measurements differ from static calibrations in significant ways. Foremost among these is time scale: dynamic compression experiments typically last no more than 100–1000 ns, which means reflectance must be measured millions to billions of times faster than in static measurements. Furthermore, diffusion limitations lead to strong thermal gradients, making it difficult to associate dynamic calibrations with specific temperatures. Dynamic experiments also tends to use one-dimensional compression, while diamond anvil cell measurements are usually quasi-hydrostatic,[1] so there may be difficulties in comparing mechanical states. If gold sensors are ever to be used in dynamic compression experiments, they have to be calibrated in dynamic compression experiments.

Figure 3.1 shows the conceptual implementation of an embedded gold sensor in a dynamic compression experiment. The sensor would be deposited onto an optical window and attached to a sample exposed to shock or ramp wave compression, probing the pressure and temperature of the sample-window interface. To characterize this state, the sensor would be illuminated with an intense white light source. Light reflected from the sensor would be delivered to a spectrometer, separating the reflected signal by wavelength. This linear image

[1]Since no pressure medium[38] was used, the results described in the previous chapter cannot even be classified as quasi-hydrostatic.

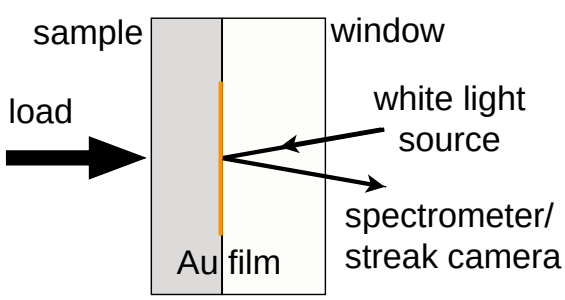

Figure 3.1. Conceptual gold sensor layout

would then be dispersed temporally by a streak camera, forming a two-dimensional image $I(\lambda, t)$. Normalizing this image by a reference image $I_0(\lambda, t)$ taken prior to compression eliminates all constant and reproducible contributions (light source, optical path, etc.) of the reflectance measurement. Assuming reproducible background levels $B(\lambda, T)$ for a fixed camera configuration (sweep rate, gain, etc.), the dynamic reflectance ratio is:

$$Q(\lambda, t) \equiv \frac{I(\lambda, t) - B(\lambda, t)}{I_0(\lambda, t) - B(\lambda, t)}. \tag{3.1}$$

Ideally, analysis of $Q(\lambda, t)$ should reveal the sensor's temperature. Sensor pressure may also be determined from such analysis, but velocimetry techniques are better suited to this task; consistency between the two diagnostics would obviously be important.

This chapter describes dynamic assessments of gold temperature sensors using plate impact experiments. Section 3.1 presents details of time-resolved reflectance measurements. Section 3.2 discusses dynamic gold sensor tests at room and elevated temperature under direct impact. Section 3.3 summarizes known problems with the dynamic measurements.

3.1 Time-resolved reflectance measurements

Reflectance is a conceptually simple measurement given a light source spanning the spectral region of interest. This is not a trivial matter in time-resolved measurements, which demand far brighter sources than static measurements. Furthermore, the normalization shown in Equation 3.1 assumes that the light source behaves reproducibly; if this is not the case, the measurement is a combination of sensor and source changes. A significant portion of this project was spent searching for intense, broad spectrum light sources. Highlights of this search are given below.

- A point source Xe flash lamp (Oriel) was used at the beginning of the project. This produced reasonable amounts of light across the visible spectrum, but the emission was not at all smooth. Most of the signal was concentrated in peaks characteristic of xenon, with a much smaller (10×) continuum superimposed on the peaks. The position of the peaks did not change, but the relative amplitude varied each time lamp was flashed.
- Compact diode lasers with 50–100 mW output (Coherent OBIS series) became available midway through the project. Several of these lasers were tested for this project and found to be quite suitable for measurements at discrete wavelengths. This method was never adopted, however, because the number of visible wavelengths (3–4) did not seem sufficient to meaningfully probe the reflectance ratio of gold.
- An extremely powerful light source known as the "MegaSun" (Prism Scientific) was found at the Nevada Test Site and transferred to Sandia for testing. This source is essentially three xenon flash lamps (in series) driven by a kilowatt pulsed power system. Tests with the MegaSun indicated its emission spectrum was quite smooth, and the

source was noticeably brighter than standard flash lamps, though only a tiny fraction of the MegaSun's output could actually be coupled to the reflectance experiments. The sheer size and potential safety hazards associated with the MegaSun made it difficult to use.

- Several evaluations of a supercontinuum laser (NKT Photonics SuperK) were made during this project. This source drives a series of ultrashort, high-power infrared pulses through a long optical fiber. Due to various nonlinear processes, the fiber's outputs a continuous spectrum from 2000 nm down to roughly 500 nm. The source is extremely bright yet fairly compact, which would be ideal for dynamic reflectance measurements. However, variability between pulses was found to be too large for this work (Figure 3.2).

- A laser-driven light source (LDLS) obtained from Energetiq was found to be almost ideal for this project. Using a rapidly pulsed infrared laser, this source maintains a small plasma inside a pressurized xenon cell, creating a very broad spectrum light source.

The LDLS was selected as the best light source for dynamic reflectance measurements in this project. Figure 3.3 shows a photograph of the EQ-99 model used for testing. A fiber-coupled version, the EQ-99FC, was obtained for the actual experiments.

Specular reflectance measurements were made with a two-fiber "bug" probe (Figure 3.4). Light from the LDLS was delivered to the probe's "send" fiber, positioned symmetrically with the receive fiber about the axis of a collimating lens. Light exiting the send fiber emerges collimated from the probe at a small angle from the optical axis. Reflections from the gold sensor return to the probe and are refocused onto the receive fiber for dynamic measurements. For optimal light coupling, 0.40 mm core fibers were used for delivery and collection. The bug probe was found to be extremely efficient, often 50% or better, but very sensitive to alignment with the gold sensor. Precise tilt and pan control of the probe was implemented using Thorlabs mount, maximizing total light return while ensuring that the probe beam (5–6 mm in diameter) remained centered on the sample. To minimize the effect of free surface reflections, most experiments used windows with a broad spectrum anti-reflection coating.

After several iterations, the dynamic reflectance system shown in Figure 3.5 was constructed for use at the Dynamic Integrated Compression Experiment (DICE) facility. Soon after the LDLS light source was selected, it was discovered that photocathode gating in the streak camera was mandatory; an EG&G camera (Livermore Operations configuration) was found to be suitable for this purpose. Light returning from the reflectance probe was sent into a grating spectrometer, converting the fiber input to a line image of varying wavelength. The line image was directed onto the photocathode of the streak camera, converted to an electronic line image, and rapidly swept to generate a two-dimensional image at the output phosphor. Time and wavelength variations in the reflectance signal are encoded into the axes of this image. After exiting the streak camera, the image passed through a micro-channel

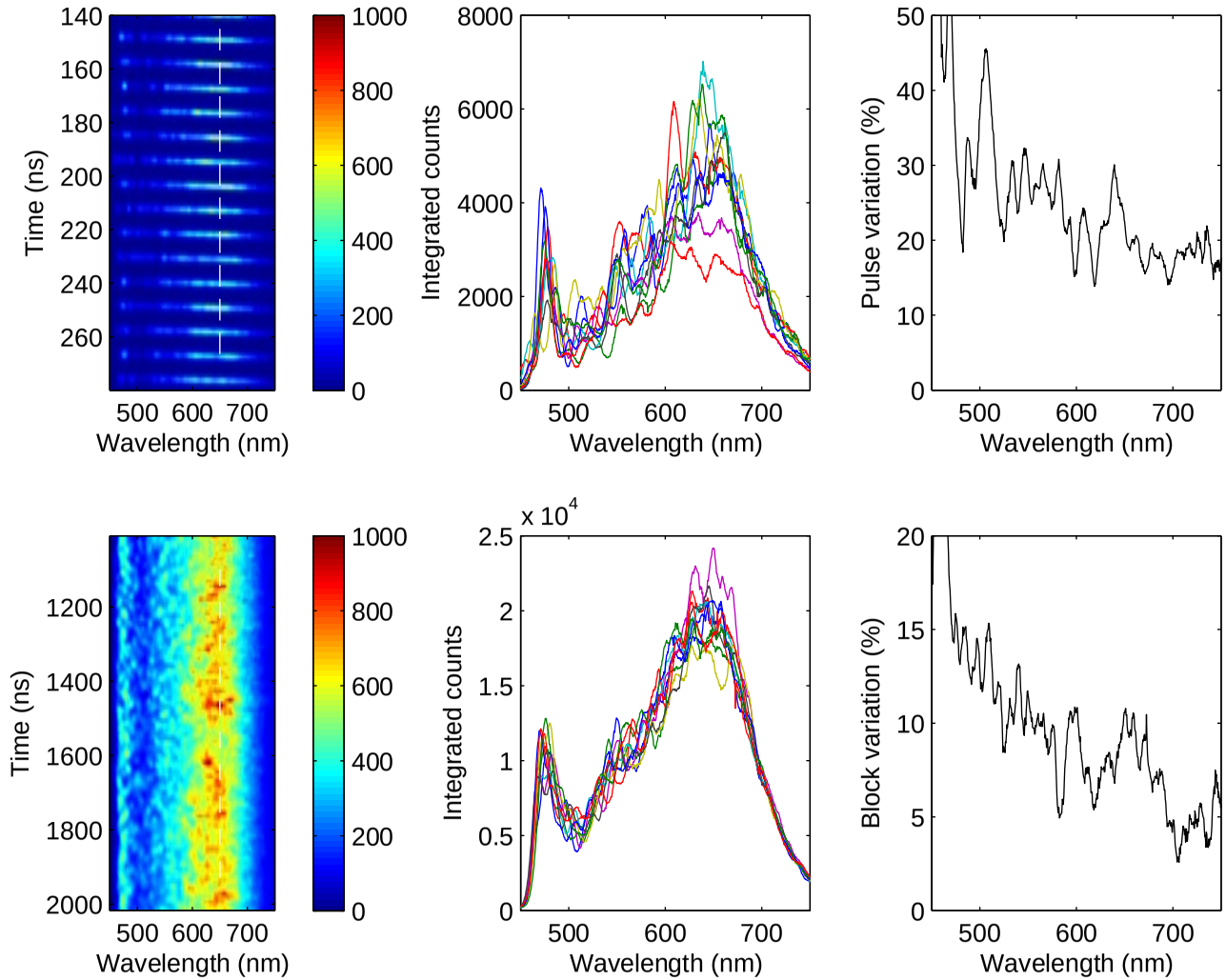

Figure 3.2. Evaluation of the SuperK laser as a light source reflectance. The left plots are streak camera spectra of the supercontinnum source after reflection from a gold target at two sweep rates. The middle plots show time-averaged spectra extracted from each image. The plots on the right show the statistical variation between laser pulses.

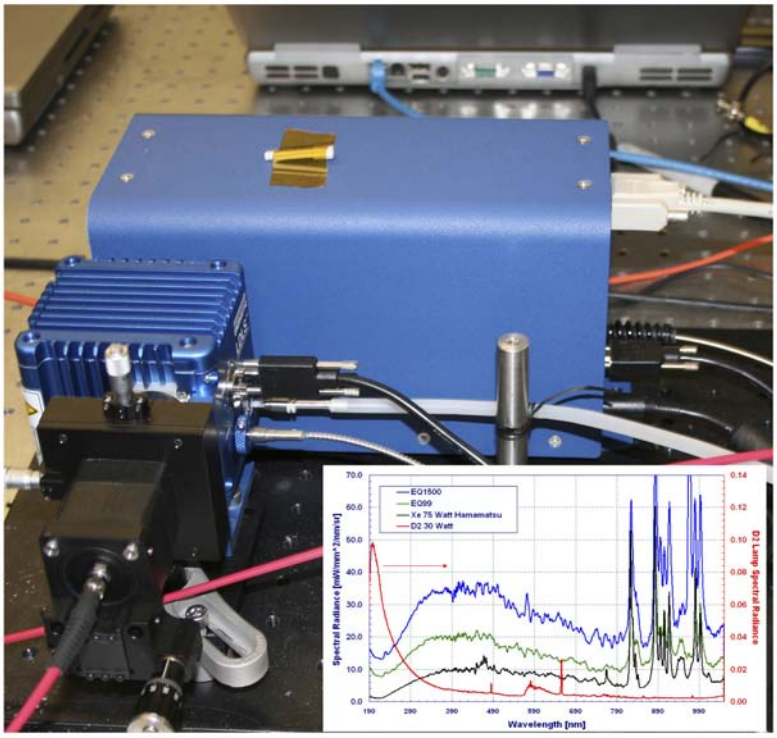

Figure 3.3. A laser driven light source (LDLS) was used as a white-light source for dynamic reflectance measurements. The larger blue box in the photograph contains a pulsed infrared laser, which maintains a small xenon plasma inside the smaller blue box. The inset shows characteristic spectra of LDLS sources in comparison with standard xenon and deuterium lamps.

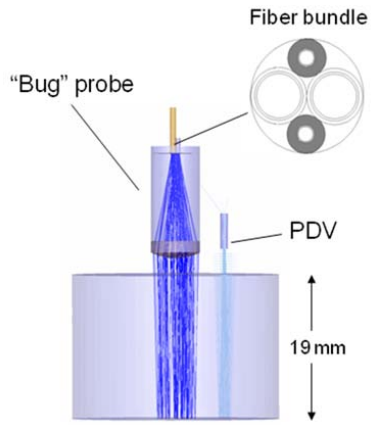

Figure 3.4. Two-fiber "bug" probe for dynamic reflectance measurements (courtesy of Special Technology Laboratory, NSTec). The separate PDV probe and spare bundle fibers (meant for VISAR) were not used in this project.

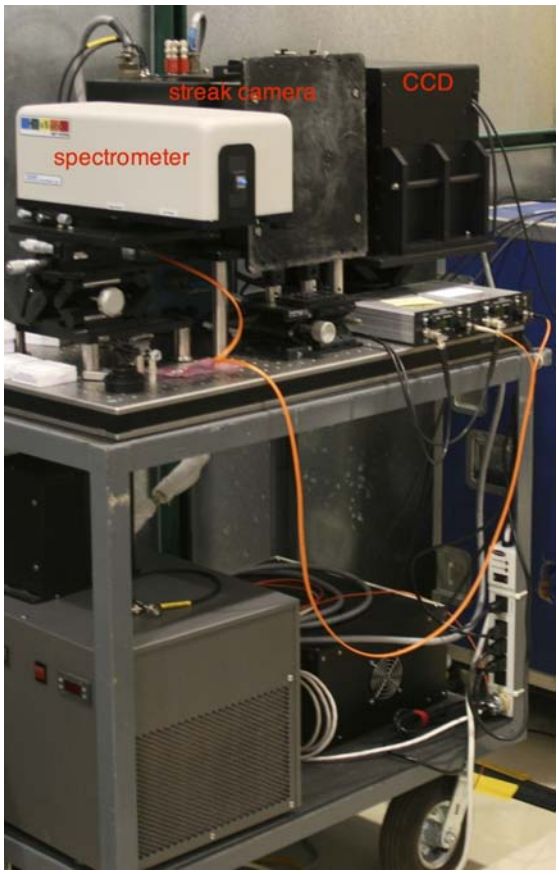

Figure 3.5. Dynamic reflectance system at DICE

plate (for amplification) and was recorded on a cooled CCD array. Background and reference measurements taken prior to the experiment were used to calculate dynamic reflectance ration (Equation 3.1).

Gold sensors for dynamic experiments were sputtered onto polished sapphire windows with no adhesion layer, which would contaminate optical measurements made through the window. Deposition occurred at room temperature on windows had been vapor degreased, rinsed with acetone then isopropanol, blown dry with nitrogen, cleaned with Alconox, rinsed with deionized water, boiled in hydrogen peroxide for 15 minutes, and finally rinsed with deionized water. With this treatment, gold coatings were found to be stable but fragile, so absolutely no physical contact was permitted. Initially, a 100 nm gold layer (verified by profilometry on a silicon witness plate placed in the sputtering chamber) was deposited on 90% or more of the window's surface. This was later changed to a 300 nm coating for better opacity, and the diameter was reduced to nominally 5 mm to aid probe centering. Gold sensors were not annealed prior to dynamic measurements. Ellipsometry was performed on one sample from each coating batch to check for consistency. Previous studies of films created by the same process found a density of 18.4±0.6 g/cc, about 4.5% lower than bulk gold (19.3 g/cc).

3.2 Direct impact experiments on gold films

Direct impact experiments (Figure 3.6) were used to subject gold sensors to known dynamic states. In these experiments, a sapphire impactor was launched onto a gold-coated sapphire window inside an evacuated target chamber. Being thinner than 0.001 mm thick, the gold sensor plays no thermo-mechanical role in the experiment, but instead rapidly equilibrates with sapphire impactor/window surroundings. The sensor's particle velocity is precisely half of the projectile velocity, measured with shorting pins immediately prior to impact, and can be used with the known mechanical properties of sapphire[39] to infer pressure. Symmetry also constrains the sensor temperature to be halfway between the impactor and window temperature. Sapphire undergoes negligible shock heating under elastic compression,[5] so far from the impact surface the impactor temperature T_1 and sensor/window temperature T_2 remain essentially unchanged. Diffusion near this surface is the same in both directions, so the sensor temperature after impact is:

$$T = \frac{T_1 + T_2}{2}. \tag{3.2}$$

Strictly speaking, the sensor requires some time to thermally equilibrate with its surroundings.[40] Assuming a limiting diffusivity of 10^{-5} m^2/s, the characteristic diffusion time (Equation 1.2) for a 300 nm thick gold sensor is 9 ns.[2] The impact experiments were designed to maintain one-dimensional compression for at least 1000 ns, so the sensor so has ample time to reach its equilibrium state.

[2]Gold has a diffusivity of 10^{-4} m^2/s, while c-axis sapphire is approximately 10^{-5} m^2/s.

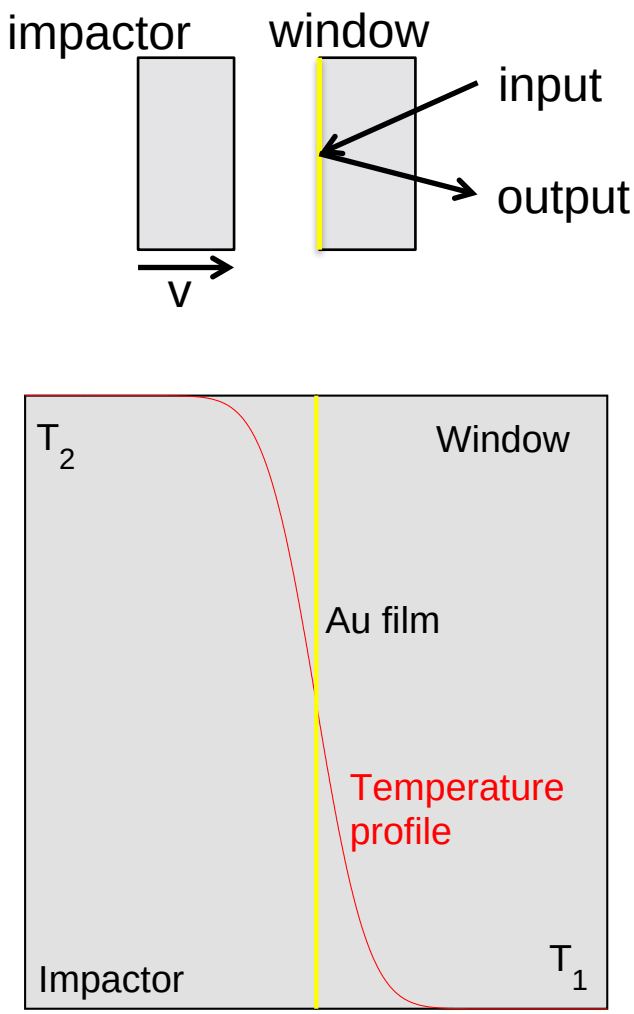

Figure 3.6. (above) Direct impact experiment layout. (below) Mechanical and thermal diffusion symmetry forces the gold sensor temperature precisely midway between the impactor and window temperatures.

Table 3.1. Summary of impact experiments at the Sandia DICE facility

Experiment	Impact velocity (m/s)	Pressure (GPa)	Impactor temperature (C)	Coating batch
DG225	325±1	7.3	25±2	1
DG241	327±1	7.3	300^{+0}_{-10}	2
DG246	151±1	3.4	25±2	2
DG247	153±1	3.4	300^{+0}_{-10}	2

Preliminary gold experiments were performed at National Security Technologies "boom box" in Santa Barbara, CA and the Shock Thermodynamic Applied Research (STAR) facility. Since the sample preparation and reflectance measurement evolved dramatically during the course of this project, these early measurements are difficult to compare with later results and have been omitted. Discussion instead focuses on impact experiments on the DICE 3" gas gun, summarized in Table 3.1. Half of the experiments were performed using the standard hardware design shown in Figure 3.7. The remaining experiments used the heated impactor design described below.

Heating the impactor prior to launch allows the gold sensor to be exposed to a dynamic temperature and pressure without unintentional annealing. The static heating capability shown in Figure 3.8 was developed for this purpose. An electrical feedthrough carrying power and thermocouple signals was added to the breech plug using a DB-9 style connector; this connection is automatically severed by projectile launch. A resistive heater embedded into the front aluminum face of the projectile slowly heated the sapphire impactor to a peak temperature of 300° C. Heating was started at ≤100 millitorr chamber vacuum to minimize the thermal loading and maintained for at least an hour (at 300° C) prior to launch. Macor layers thermally isolated the projectile body, which was found to never exceed 30° C during thermal cycle testing. Two thermocouples clamped to the sides of sapphire impactor monitored its temperature throughout the heating process. The impactor face temperature was found to be no more than ten degrees lower than the side thermocouple readings and never higher.

Figure 3.9 shows the dynamic reflectance ratio images obtained in experiments DG225, DG241, DG246, and DG247. The horizontal axis of these images was calibrated with bandpass filters prior to the experiment; the vertical axis was calibrated with an optical comb (not shown) recorded during the measurement. The vertical axis was shifted to place impact, evident by a massive signal reduction across the spectrum, at time $t = 0$. Apart from this drop, all four measurements showed similar spectral variations, where the reflectance ratio on the blue side of the spectrum exceeds that on the red side.

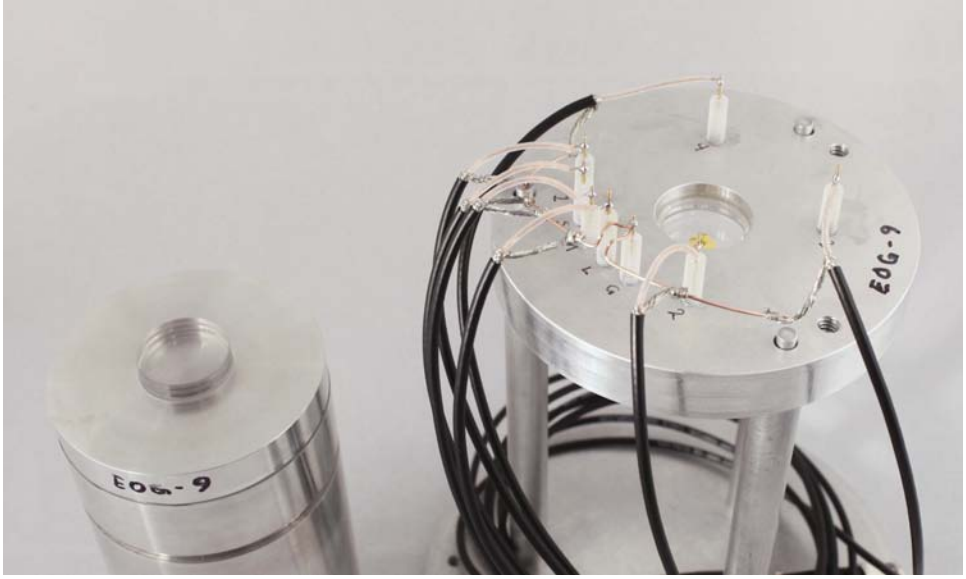

Figure 3.7. Standard impact experiments on the DICE 3" gas gun. The projectile (left) carries a sapphire impactor at room temperature. The target plate (right) has a identical sapphire window with gold dot on one side and an antireflective coating on the other. Electrical cables on the target plate are used to measure projectile velocity and tilt.

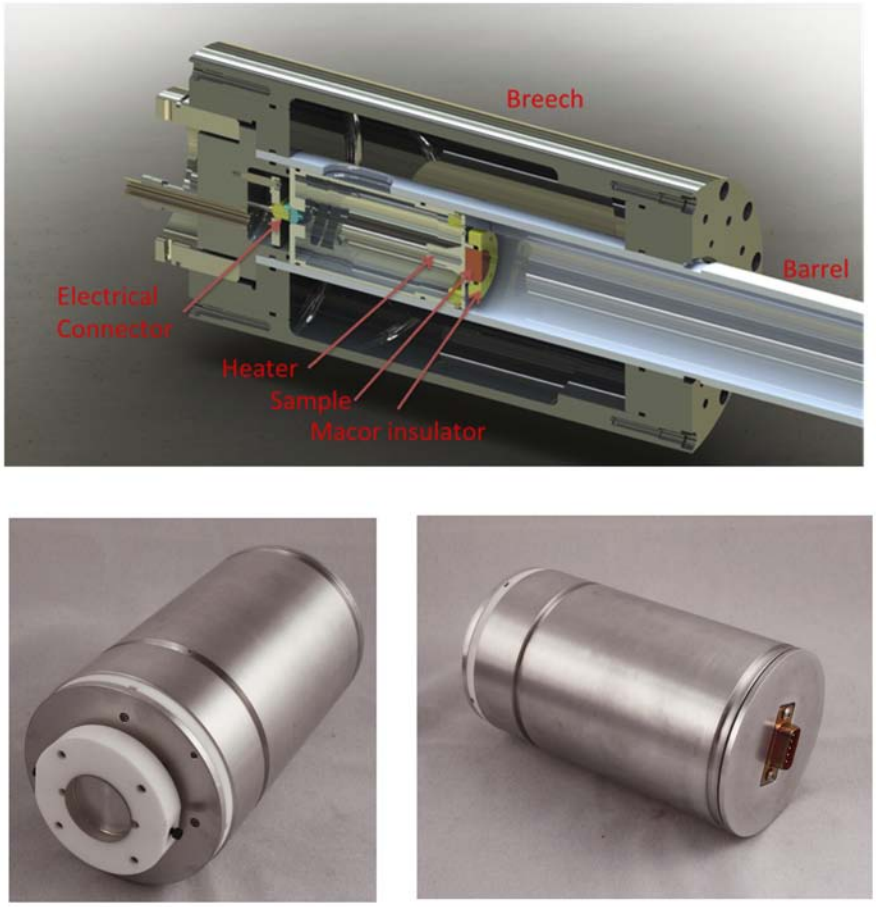

Figure 3.8. Heated projectile for the DICE gas gun. The top image shows a cross section of the projectile in the wrap around breech. The bottom left image shows the front of the projectile with the Macor thermal isolation buffers. The bottom right image shows the rear of the projectile, where electrical signals (heater and thermocouples) pass through the DB-9 pin connector for quick disconnection at launch.

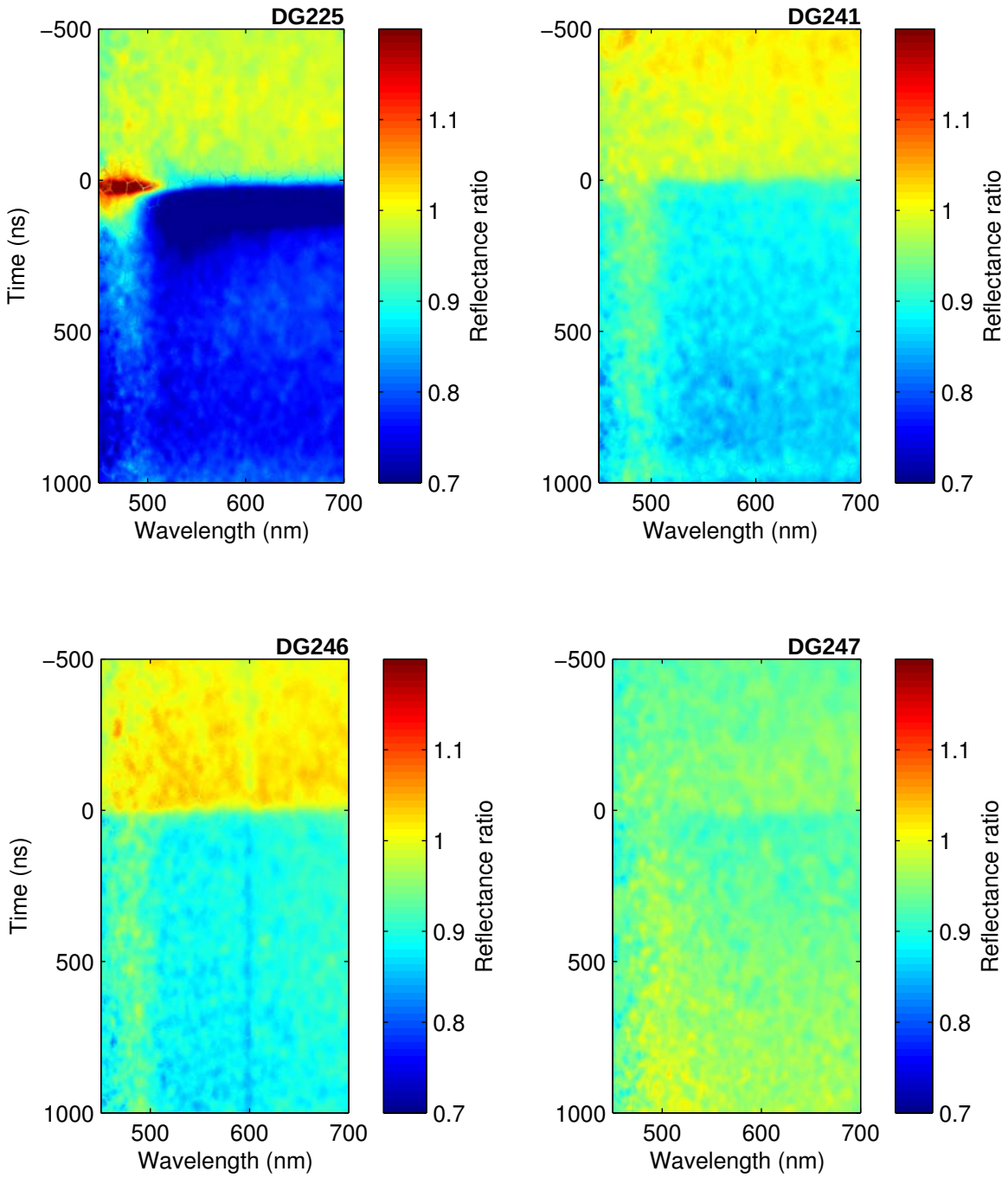

Figure 3.9. Dynamic reflectance ratio images obtained from direct impact of gold. Images on the left were obtained from a room temperature impact, while images on the right were from heated impact experiments (300° C). Impact pressures were 7.3 GPa (upper images) and 3.4 GPa (lower images).

The top plot in Figure 3.10 shows vertical slices of the reflectance image from experiment DG246 at three wavelengths. The 475 nm slice is higher than the 550 nm and the 650 nm slice; the 650 nm slice is somewhat higher than the 550 nm slice. This spectral variation is better visualized as horizontal slices of the reflectance image. The lower plot of Figure 3.10 shows time averaged (200 ns duration) slices from experiment DG246. These spectra are certainly smoother than than individual slices, but it is evident that some of the unwanted features (such as the 600 nm region) are not random, a subject discussed more fully in the next section. With sufficient smoothing and some imagination, the dynamic reflectance ratio curves that are qualitatively similar to heated gold at ambient pressure.

Experiment DG225 is noticeably different than the others: a strong spectral feature appears at impact and seems to dissipate with time. This rapid feature may indicate an impact flash caused by gas trapped between the impactor and sample. Such flashes may result from residual gas in the gun barrel or leakage around the projectile O-rings; both effects have been observed on this gun in the past. Residual gas would have been less likely in the heated experiments because of the extended pumping time allowed for thermal stabilization. After experiment DG225 was completed, the barrel of the 3" gun was damaged during a failed heated impactor test, so the later three experiments were performed with a different barrel. As such, it is impossible to know if gas leakage was more or less probable in experiment DG225 than in later experiments.

3.3 Known problems

Dynamic reflectance measurements at the conclusion of this project were based on the LDLS, collimating bug probe, and a particular streaked spectroscopy configuration. Although successful measurements were obtained, significant shortcomings of all three subsystems were identified. These problems and sample preparation issues are documented here as an aid to future users of dynamic reflectance, gold-based or otherwise.

While the LDLS spectral coverage is quite satisfactory for this project, the light source is not truly steady. Instead, 100–200 kHz emission variations were detected and confirmed with the vendor as the result of heating/cooling cycles of the xenon plasma. Initial characterizations suggested that the peak-trough variations were less than 1%, so this variation was ignored for some time. Later on, variations of 5–10% were observed, violating assumptions of a steady light source. Subsequent analysis attempted to compensate for this behavior, but the corrections could not be perfected without source monitor measurements during each experiment (which were not made). The LDLS was sufficiently bright for the present study, where measurements were streaked over several microseconds, but would not suffice for Z experiments, where sweep rates are typically ten times faster.

Probe design is often a tradeoff between efficiency and robustness, and the bug probe was selected with a strong emphasis on the former. High probe efficiency made measurements feasible with the LDLS, but alignment sensitivity was problematic for two reasons. Setting

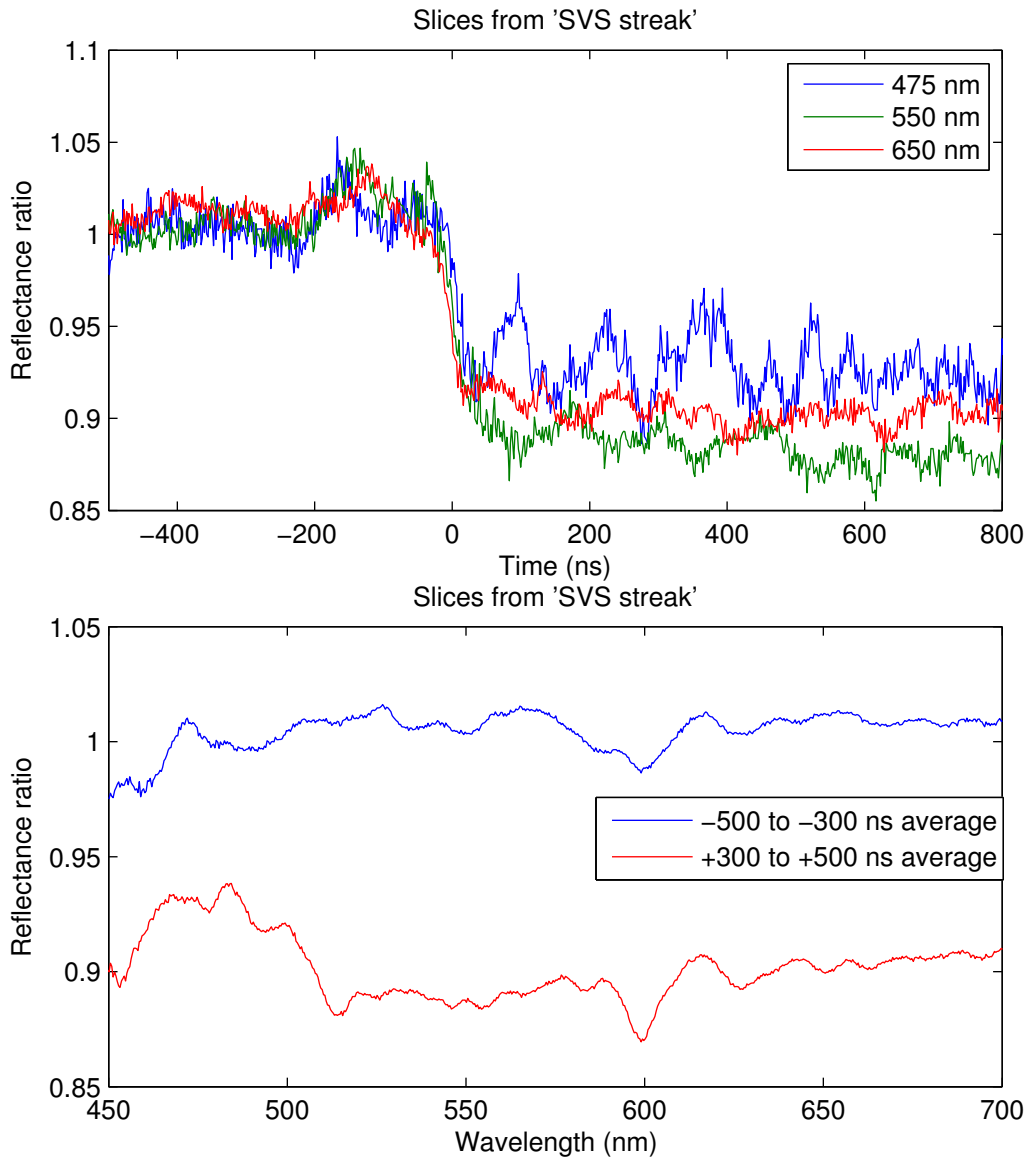

Figure 3.10. (upper) Fixed wavelength slices of the reflectance ratio image in experiment DG246. (below) Time averaged spectra extracted from the same image.

up the bug probes was very time consuming, and it is unlikely that multiple probes could be installed quickly enough for deployment at Z. Furthermore, the tilt sensitivity complicates interpretation in a random way—light levels always decreased at impact, but by an unpredictable amount—that adds another degree of freedom to spectral analysis. Efforts were made to transition to a single fiber probe, sending and receiving light on the same fiber, but these proved to be unsuccessful.

For compactness, a transmission grating spectrometer with lens imaging (Acton) was used in this project to disperse reflected light into separate wavelengths. Although the output focus of this spectrometer was extremely sharp, multiple reflections were found to exist. Lasers passed into the spectrometer emerged as multiple line outputs, similar to multiple diffraction orders but at incorrect locations; similar effects presumably occur in broad spectrum measurements but are much harder to identify. These defects appeared to be on the order of 1% of the source feature, so an alternative spectrometer design is recommended.

Virtually all streak camera measurements contained a hexagonal "chicken wire" feature, an artifact of the micro-channel plate. This observation is not unusual, but is expected to cancel out of ratio measurements if spatial variations in the system sensitivity (camera + MCP + CCD) are reproducible. This cancellation was highly imperfect, leaving noticeable mesh artifacts in the ratio images. The problem is most evident in the DG225 image of Figure 3.9 but can be found in close inspection of the other three images. The overall texture of the ratio images also mimics a hexagonal pattern. Local smoothing partially alleviates but does not fully remove the problem, and methods for digitally masking the wires were not found to be effective. This particular streak camera produced unusually strong hexagonal artifacts, so simply changing to a different system might solve this problem.

Although sample preparation (sputtering, electroplating, etc.) was known to affect the optical properties of gold, a startling discovery was made in the last year of the project. Even with the same coating protocol, minor changes in the optical properties were observed at low photon energy (Figure 3.11). Based on previous studies,[33] this difference is probably due to grain size variations between sputtering runs, which could be attributed to the lack of substrate temperature control during deposition. This finding reinforces the need for batch characterization.

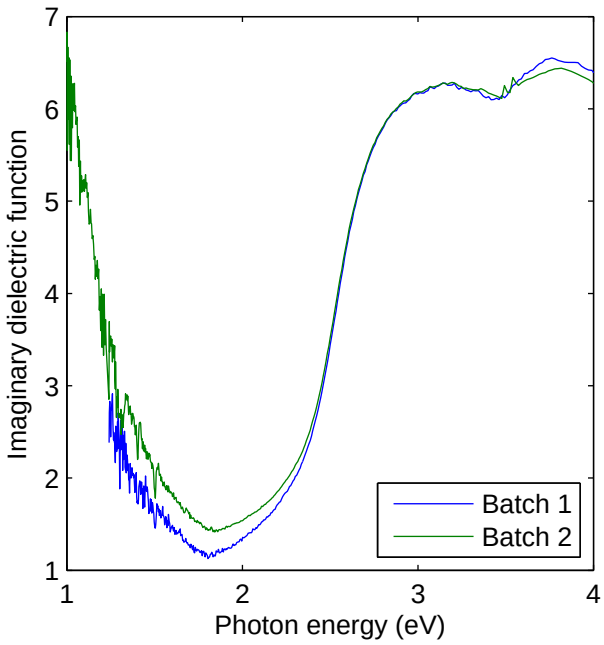

Figure 3.11. Consistency between gold coating batches

Chapter 4

Minimal gold model

The preceding chapters demonstrate that the reflectance spectrum of gold clearly changes with temperature and pressure. Inferring temperature from reflectance measurements isn't nearly as straightforward. There is no single reflectance spectrum for gold, but rather a range of spectra that vary with the host index through which the measurement is performed. Air/vacuum, diamond, and sapphire were used in this project, and future window materials of interest include lithium fluoride, magnesium oxide, quartz, and cubic zirconia. With host indices n^*=1–2.4, the apparent reflectance of gold varies dramatically between heated ellipsometry, diamond anvil cell, and direct impact measurements. Window-specific calibrations could be attempted, but tremendous redundancy would be needed to span all temperatures and pressures of interest.

The optical properties of gold can be described in a variety of representations. Table 4.1 summarizes these representations and their interrelationships. The most fundamental representation, dielectric function $\tilde{\epsilon}$, is the basis for theoretical models of optical response. The refractive index $\tilde{n}$ is more convenient for experimental applications, so this is the quantity typically found in material tabulations.[25] Given one complex variable ($\tilde{\epsilon}$ or $\tilde{n}$), the other variable can be determined with no loss of information. The same is not true for reflectance R, which combines the material's index with a host index n^*. Although Kramers-Kronig analysis[41] can recover the complex refractive index in some cases, measurements of R over a limited spectral range are insufficient to determine $\tilde{\epsilon}$ or $\tilde{n}$ accurately. Furthermore, the dynamic measurements described in Chapter 3 measure reflectance ratio, which is even further removed from $\tilde{\epsilon}$.

This chapter describes an empirical model for gold's optical properties using a minimal number of adjustable parameters. For a given set of parameters, the behavior of gold can be formulated in any representation for comparison with experimental data. Ultimately, the model is a pathway for reducing gold sensor measurements to temperature. Section 4.1 provides an overview of the model. Section 4.2 uses heated ellipsometry and diamond anvil cell measurements to probe variations of model parameters with temperature and pressure. Section 4.3 uses these parameter studies to estimate reflectance ratio spectra that would occur under dynamic compression and compares the predictions with the direct impact experiments.

Table 4.1. Relationships between dielectric function, refractive index, reflectance, and reflectance ratio.

$$
\begin{array}{ccc}
 & \text{Dielectric function} & \\
 & \tilde{\epsilon} = \epsilon_1 + i\epsilon_2 & \\
n = \sqrt{\dfrac{|\tilde{\epsilon}| + \epsilon_1}{2}} \;\Big\downarrow & & \Big\uparrow\; \begin{array}{l} \epsilon_1 = n^2 - k^2 \\ \epsilon_2 = 2nk \end{array} \\
k = \sqrt{\dfrac{|\tilde{\epsilon}| - \epsilon_1}{2}} & & \\
 & \text{Refractive index} & \\
 & \tilde{n} = n + ik & \\
R = \dfrac{(n - n^*)^2 + k^2}{(n + n^*)^2 + k^2} \;\Big\downarrow & & \\
 & \text{Reflectance } R & \\
Q = \dfrac{R}{R_0} \;\Big\downarrow & & \\
 & \text{Reflectance ratio } Q &
\end{array}
$$

4.1 Model overview

The optical conductivity of gold is a combination of free and bound electron effects.

$$\tilde{\epsilon}(E) = \epsilon_\infty - \frac{E_P^2}{E^2 + i\gamma E} + \tilde{G}(E) \tag{4.1}$$

Free electron (intraband) effects are described by the Drude model, which has three parameters. The plasma energy E_P is related to the square root of the free electron density, while the broadening parameter γ is inversely proportional to the mean scattering time τ; combinations of these parameters can be linked to the DC conductivity. The permittivity at infinite energy ϵ_∞ is a tunable parameter that accounts for bound electron effects not explicitly modeled (ideally ϵ_∞=0). For gold, the Drude model is the dominant contribution in the infrared spectrum.

Bound electrons are much more complicated than the free electrons, and there are a variety of ways for modeling interband transitions. The Lorentz model:[41]

$$\tilde{G}_m(E) = E_P^2 \sum_m \frac{w_m}{E_m^2 - E^2 - i\Gamma_m E} \tag{4.2}$$

considers bound electrons as masses on springs with resonance energy E_m and broadening energy Γ_m. Multiple resonances are introduced to model real materials, tuning the parameters w_m, E_m, and Γ_m to match measurements of the complex dielectric function. Single[42] and multiple[43] resonance Lorentz models have been applied to gold with varying degrees of

success. The use of more resonances provides a better fit to experimental data, but the number of parameters quickly becomes excessive. The single resonance model has six adjustable parameters (three Drude, three interband) and is effective through only part of the visible spectrum, while the multiple resonance approach has fourteen adjustable parameters but is effective deep into the ultraviolet region.

Several interband models for gold have been proposed as being more realistic than Equation 4.2. The most widely known is by Etchegoin,[44] which uses a critical point transition:

$$\tilde{G}_m(E) = C_m \left[\frac{e^{i\phi_m}}{(E_m - E - i\Gamma_m)^{\mu_m}} + \frac{e^{-i\phi_m}}{(E_m + E + i\Gamma_m)^{\mu_m}} \right] \tag{4.3}$$

at two resonances. With five parameters per resonance (C_m, ϕ_m, E_m, Γ_m, and μ_m), the complete model has thirteen potentially adjustable parameters; constraints are applied in Reference 44 to pare this down to eleven. Figure 4.1 shows the Etchegoin model optimized to a gold sensor from this project. Although the model does a reasonable job of fitting the dielectric function, individual components of the model exhibit unphysical behavior. The first interband transition, which peaks near 2.75 eV, decreases as expected at lower photon energy but eventually becomes negative. Such behavior suggests that the real conductivity ($\sigma_1 \propto \epsilon_2$) of this contribution is also negative, which is physically impossible. During optimization, the second interband feature becomes overly broad to compensate for the negative ϵ_2 contribution of the first feature, so the violation isn't evident in the complete model.

Other interband models for gold avoid negative ϵ_2 but introduce other problems. As shown in Figure 4.1, the Hopkins[45] model has three interband contributions that are always positive. However, the interband contributions are not confined to higher photon energy, but instead have a significant impact at lower energies where the Drude contribution should dominate. The Hopkins model is significantly more complicated than the Etchegoin model, though the number of parameters remains the same (eleven at ambient conditions). A gold model proposed by Rakic[46] also maintains positive ϵ_2 but requires 23 adjustable parameters!

Given that each parameter may change with temperature and pressure, a gold model with a minimum number of adjustable parameters is critical for this project. Another requirement is that the model be as physically realistic as possible, or at least be minimally unphysical—interband violations must be avoided, and interband contributions should be confined to the correct spectral range. The following model is proposed as the simplest way to model the visible properties of gold.

$$\begin{aligned} \tilde{\epsilon} &= \epsilon_\infty - \frac{E_P^2}{E^2 + i\gamma E} + E_P^2 \int_0^\infty \frac{w(x)}{x^2 - E^2 - i\Gamma E}\, dx \\ &= \epsilon_\infty - \frac{E_P^2}{E^2 + i\gamma E} + \frac{w_B E_P^2}{2a} \ln\left(\frac{E_B + a}{E_B - a}\right) \\ a^2 &\equiv E^2 + i\Gamma E \end{aligned} \tag{4.4}$$

This model simplifies a proposal by Brendel and Bormann,[47] where a continuous distribution of Lorentz oscillators defines a broad optical transition. The simple result shown in

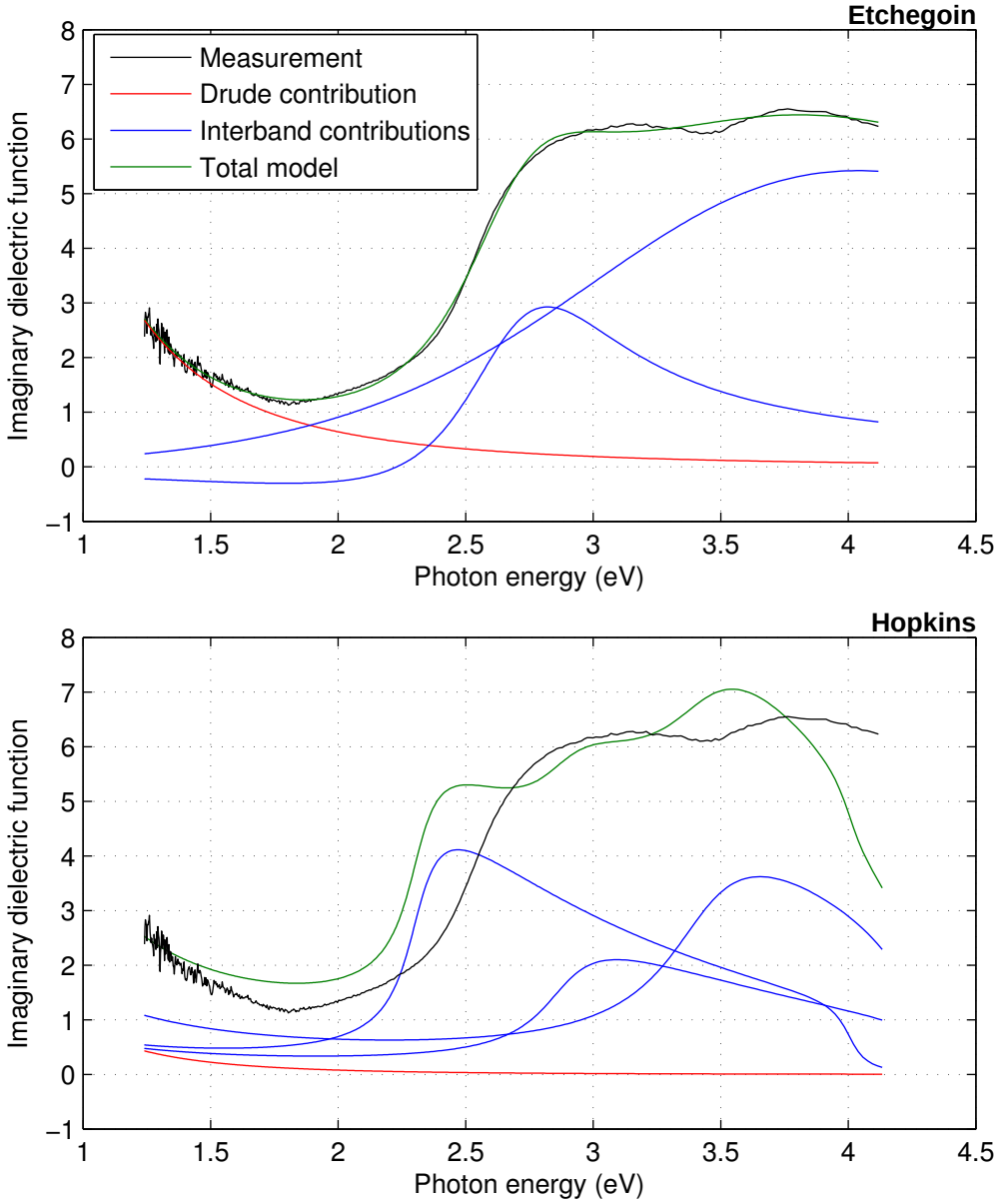

Figure 4.1. Previous interband models for gold from Reference 44 (above) and Reference 45 (below). Note that the Etchegoin model has been optimized with a measurement from this study while the Hopkins model has not.

.

Equation 4.4 assumes a simple weight function.

$$w(E) = \begin{cases} 0 & E < E_B \\ w_B & E \geq E_B \end{cases} \tag{4.5}$$

Strictly speaking, this model violates the optical sum rules[41] at infinite photon energy, but in practice the violation occurs far from the 1–3 eV range of interest. The weight function could be cut off at an arbitrarily high photon energy (*e.g.*, 100 eV) with minimal impact in the visible spectrum.

This minimal gold model has six parameters—three Drude (ϵ_∞, E_P, and γ) and three interband (w, E_B, Γ)—like the single resonance Lorentz approach yet better represents gold's broad absorption of green and blue wavelengths. Figure 4.2 illustrates this with plots of ϵ_2 for the both models along with an ellipsometry measurement from this project. The single resonance Lorentz model has not been optimized against this measurement, so the two models may differ at low energy. The more significant issue sharp peaking of the single resonance peak, which is cannot simultaneously match rapid variation at 2.5 eV and the the slow variation at 3–4 eV. Adding multiple resonances certainly helps, but discrete Lorentzians are too symmetric to represent the two interband features evident in Figure 4.1. The minimal model better simulates gold behavior because the continuous distribution turns on at a specific energy, mimicking the asymmetric shape of ϵ_2.

Table 4.2 shows the minimal model parameters obtained for optimizations of both gold batches prepared for dynamic experiments. The optimization used complex ellipsometry data, minimizing the square error of difference magnitude:

$$\chi^2 \equiv \sum_m |\tilde{\epsilon}_m(\text{measured}) - \tilde{\epsilon}_m(\text{model})|^2 \tag{4.6}$$

from the 450–700 nm (2.76–1.77 eV) wavelength range relevant to dynamic measurements. For most parameters, similar results were obtained for both samples. Key exceptions are the broadening factors, particularly free electron broadening γ, which suggests that two coating runs led to different grain sizes.[33] The plasma energy is similar to that of Ordal,[48] and the free electron broadening falls in the range of reported values for gold.[49]

4.2 Static temperature and pressure effects

Static measurements tests of the pressure/temperature dependence of parameters in the minimal gold model. However, the parameters from the analysis of static measurements do not extrapolate to the values shown in Table 4.2 at ambient conditions. Stable ellipsometry measurements require annealing, so ambient measurements may differ somewhat from the dynamic gold sensors. Static compression measurements are based on gold foils rather than sputtered coatings, so again the model parameter values will be somewhat different. This discussion emphasizes parameter *variation* with temperature and pressure, which are assumed to be characteristic of gold regardless of preparation.

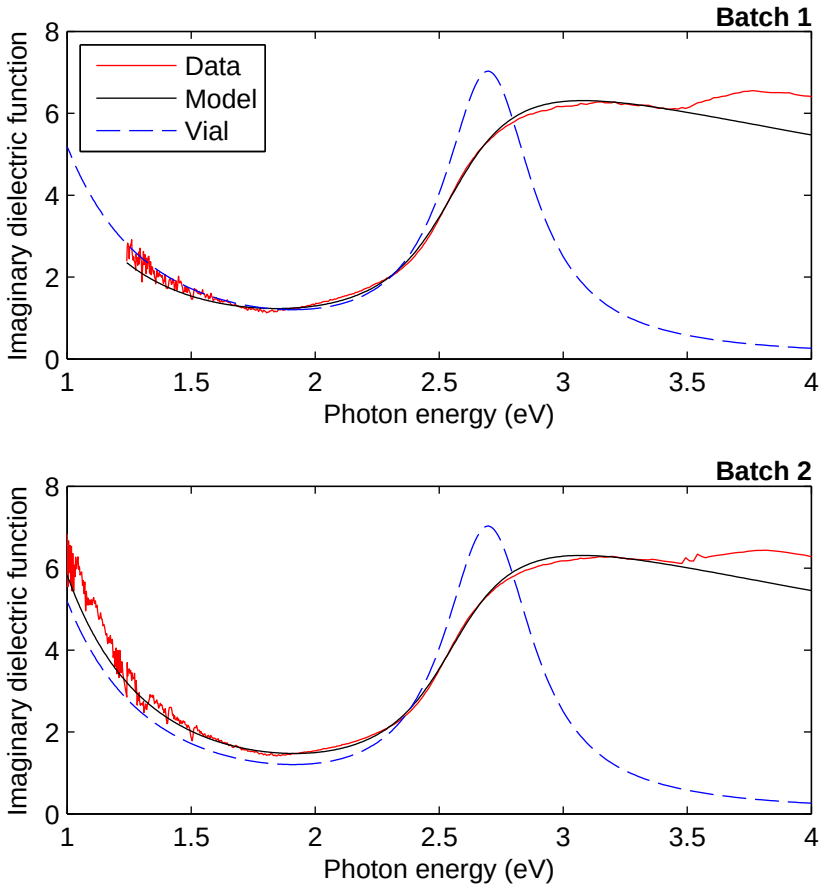

Figure 4.2. Minimal model applied to gold samples at ambient conditions. The dashed line indicates the model described in Reference 42.

Table 4.2. Minimal model parameters for different sensor batches

Parameter	Batch 1	Batch 2
ϵ_∞	1.13	1.15
E_P (eV)	8.92	8.93
γ (eV)	0.0509	0.0716
w_B	0.187	0.185
E_B (eV)	2.57	2.57
Γ (eV)	0.478	0.480

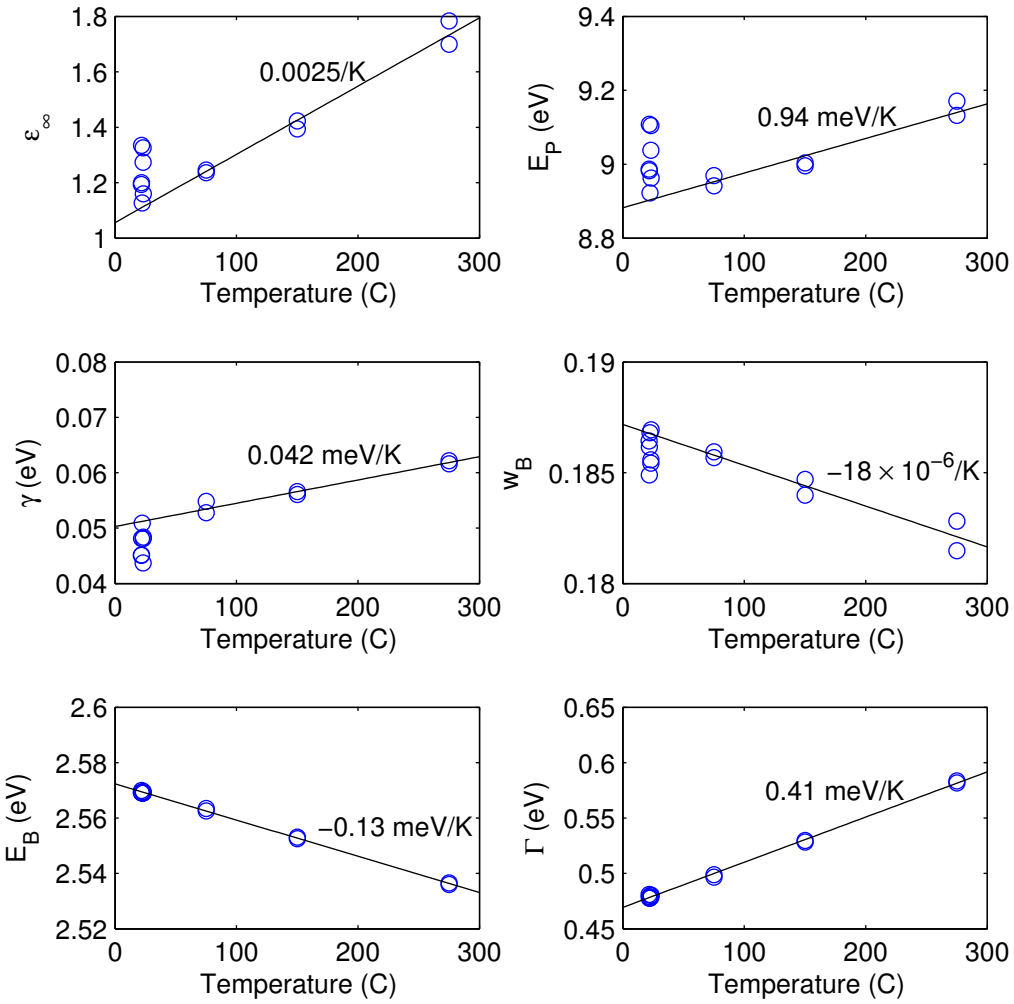

Figure 4.3. Gold model temperature trends

Figure 4.3 shows the optimized parameters for an annealed gold sensor for temperatures up to 275° C (upper plot in Figure 4.3, page 51). These optimizations are based on the complex dielectric function, minimizing the total residual as described in Equation 4.6 with respect to all six model parameters for the 450–700 nm range. Most of these parameters show a clear trend apart from some hysteresis effects at room temperature (excluded from the linear fits). Four parameters (ϵ_∞, E_P, γ, and Γ) increase with temperature while two parameters (w_B and E_B) decrease with temperature.

$$\frac{\partial \epsilon_\infty}{\partial T} = 0.0025 \text{ /K} \qquad \frac{\partial E_P}{\partial T} = 0.94 \text{ meV/K} \qquad \frac{\partial \gamma}{\partial T} = 0.042\text{meV/K}$$
$$\frac{\partial w_B}{\partial T} = -18 \times 10^{-6} \text{ /K} \qquad \frac{\partial E_B}{\partial T} = -13 \text{ meV/K} \qquad \frac{\partial \Gamma}{\partial T} = 0.41 \text{ meV/K}$$

These variations provide several physical insights about into the behavior of gold.

- Plasma energy is proportional to the square root ρ/m (density over effective mass). Heating gold reduces density as the lattice expands, so the fact that E_B increases with temperature indicates that the effective mass must be decreasing faster than ρ.
- Free electron broadening is proportional to E_P^2 divided by the DC conductivity. Conductivity in gold decreases with as $1/T$,[50] acting in conjunction with E_P so that γ increases with temperature.
- Interband weight decreases slightly with temperature, though over this range the change is minor.
- The interband edge decreases with temperature, causing absorption at lower photon energy. This is similar to results of Winsemius,[51] who reported a decreasing interband transition near 2.5 eV with temperature.
- Interbrand broadening, like free electron broadening, increases with temperature. Although the slopes differ by an order of magnitude, interband broadening is about ten times larger than free electron broadening, so the relative change with temperature (about 8% per 100 K) is very similar.

The variation in ϵ_∞ is difficult to ascribe to any specific physical principle.

Figure 4.4 shows calculated reflectance ratio spectra for gold based on the minimal model. Thermal variation of each parameter is assumed to be linear, with the slopes shown in Figure 4.3. These predictions show the behavior expected for gold: curves that increase in the blue and decrease in the red, transitioning near 500 nm. For comparison, a curve derived from Reference 15 is included with calculated curves. The model calculations under-predict maximum and minimum ratio changes, but this difference may be attributed to sample preparation. Beran describes samples as gold "shots" (presumably bulk gold) that were ground and polished by hand.

Figure 4.5 shows optimized parameters for gold foils compressed in a heated diamond anvil cell. Since DAC measurements are limited to reflectance spectra and ambient dielectric

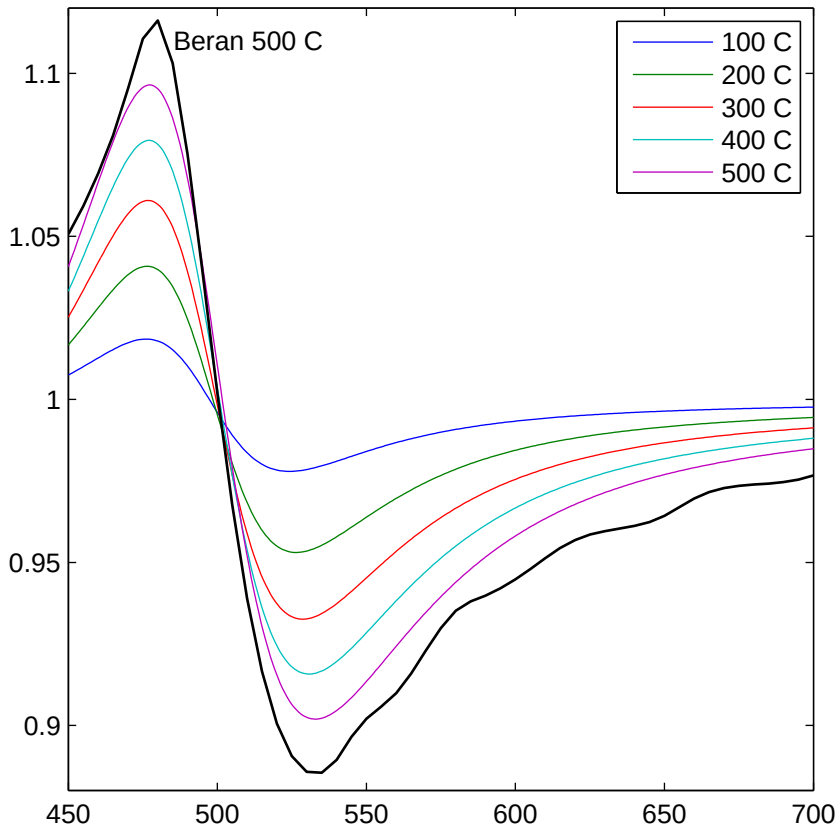

Figure 4.4. Reflectance ratio predictions for heated gold at atmospheric pressure

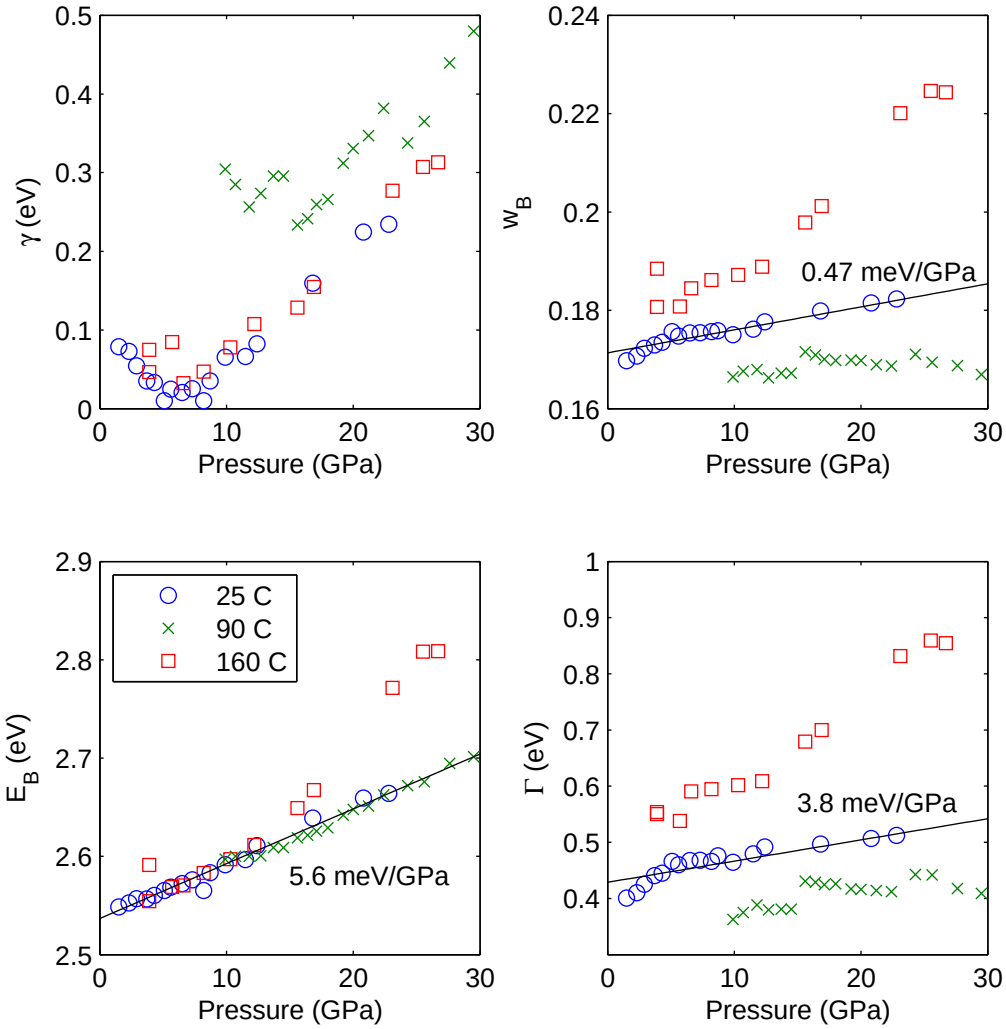

Figure 4.5. Gold parameter pressure trends. Linear fits apply to the 25° C data only.

spectrum for the foils in unknown, the ϵ_∞ parameter was arbitrarily fixed at 1 and E_P at 9 eV. Within the optimization, the refractive index of diamond[52] was treated as a function of wavelength no imaginary component. The residual:

$$\chi^2 \equiv \sum_m |R_m(\text{measured}) - R_m(\text{model})|^2 \tag{4.7}$$

was determined over the 450–700 nm range. Three of the adjustable parameters (w, E_B, and Γ) increase monotonically with pressure, while the fourth (γ) initially decreases with temperature. To understand the latter behavior, recall that γ is proportional to $\rho^{1/2}m^{-1/2}\sigma^{-1}$. Density and conductivity increase with pressure, which could indicate that conductivity initially increases faster than density. Effective mass of the free electron could also play a role in the non-monotonic behavior of γ.

As an initial characterization, assume that only the three monotonically increasing parameters are important for reflectance spectrum calculations. Using solely the room temperature data, the pressure derivatives of these variations are:

$$\frac{\partial w}{\partial P} = 470 \times 10^{-6}\ /\text{GPa} \qquad \frac{\partial E_B}{\partial P} = 5.6\ \text{meV/GPa} \qquad \frac{\partial \Gamma}{\partial P} = 0.47\ \text{meV/GPa}$$

determined from the linear fits shown in Figure 4.5. The remaining derivatives are assumed to be zero.

4.3 Impact experiment comparison

Reflectance ratio estimates for the direct experiments can be generated from the parameter derivatives obtained in static measurements:

$$\vec{p} \equiv [\epsilon_\infty\ E_P\ \gamma\ w\ E_B\ \Gamma\ ]^T$$
$$\vec{p} \approx \vec{p}_0 + \frac{\partial \vec{p}}{\partial T}(T - T_0) + \frac{\partial \vec{p}}{\partial P}(P - P_0) \tag{4.8}$$

where cross-derivatives and higher-order terms are neglected. Given a temperature/pressure state and host index (sapphire,[53] in this case), the ideal reflectance ratio for an embedded gold sensor can be determined; selecting the correct state should optically match the ratio spectrum measurement. However, sensor tilt complicates matters, allowing the reflectance ratio to appear systematically higher or lower than parameter optimization would allow. If tilt effects are wavelength independent, a single scaling parameter can be used to match model calculations to a tilted measurement over k wavelengths.

$$Q_k = \underbrace{\frac{R_k}{R_{0_k}}}_{y_k} \times A \tag{4.9}$$

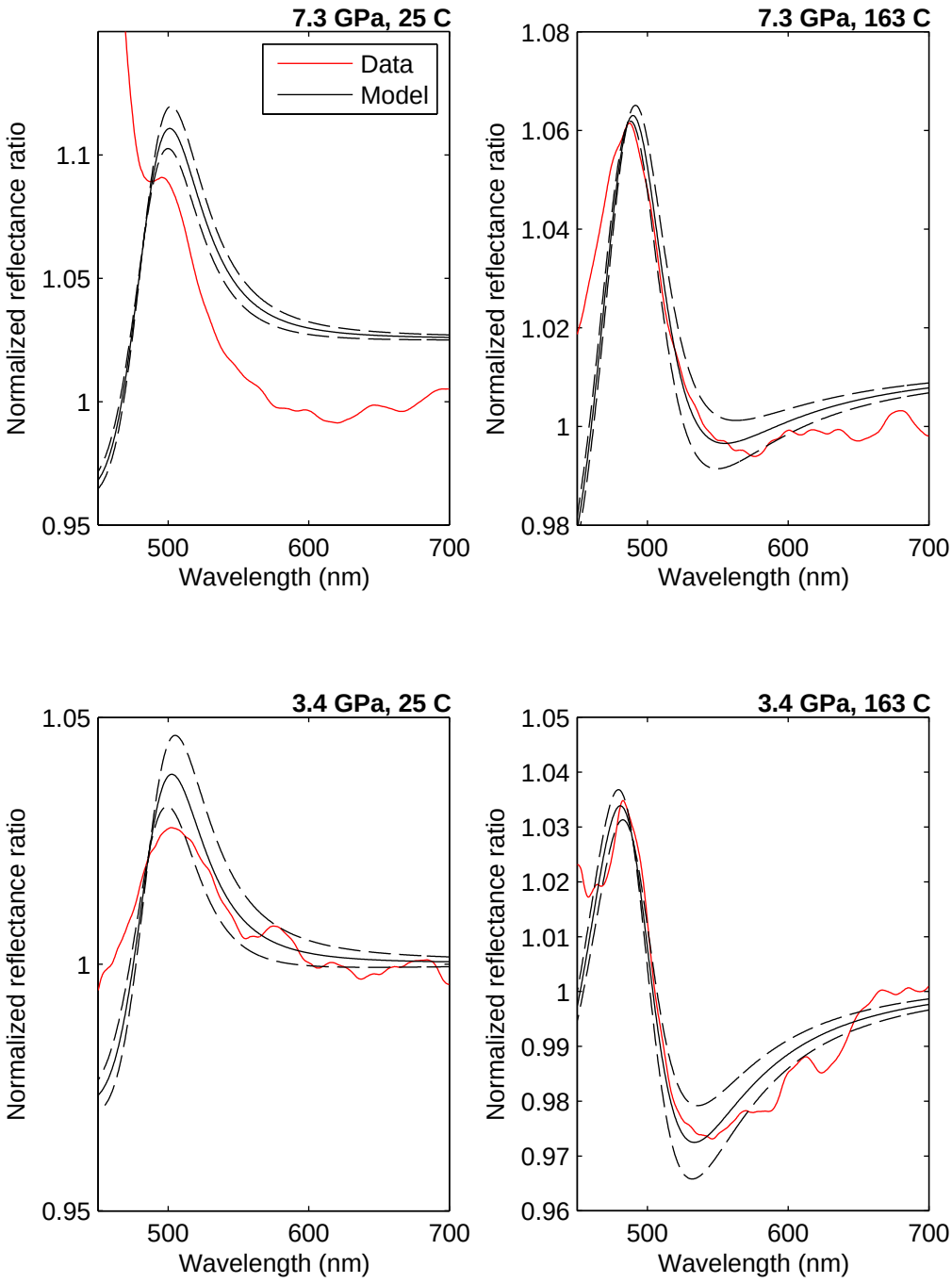

Figure 4.6. Minimal model applied to direct impact measurements of gold. Dashed lines indicate ±20° K temperature variations in the model. Dynamic measurements are normalized to keep spectra near unity (despite tilt) for comparison and model calculates are scaled to match (Equation 4.9).

The scaling factor A can be determined by linear least squares (matrix division):

$$A = \vec{y} \setminus \vec{Q} \tag{4.10}$$

as implemented in MATLAB's backslash operator.[54]

Figure 4.6 shows normalized reflectance ratios calculated from the minimal gold model, using the temperature and pressure derivatives described in the previous section. Apart from a wavelength-independent scaling for tilt, no optimization was used to match the model with impact data. In three cases, the model shows plausible agreement with the measurement, particularly for the heated experiments. The model performed poorly against the 7.3 GPa measurement at room temperature, perhaps because of the non-monotonic behavior of γ with pressure at lower temperatures (Figure 4.5); lacking a simple description for this behavior, pressure variations in this parameter are not currently handled in the minimal gold model. The experiment in question (DG225) may also have experienced a trapped gas flash that could account for some of the discrepancy.

As a test of temperature sensitivity, spectra for temperatures above and below the anticipated temperature were also generated. These spectra, indicated by dashed lines in Figure 4.6, indicate that 20° C temperature changes are likely resolvable with a gold sensor. This is most evident in the bottom right plot, where the shape of the minimum well (500–600 nm) is noticeably different for 143° C, 163° C, and 183° C.

This page intentionally left blank.

Chapter 5

Summary and future work

The fundamental goal of this project was to develop an optical temperature sensor for eventual deployment in Z experiments. Work completed thus far indicates that gold sensors inside a dynamic compression experiment can detect changes that would be indistinguishable to other temperature diagnostics. The primary scientific challenge is and will continue to be calibration, separating pressure-induced changes from temperature-induced changes. A variety of technical challenges must also be addressed.

Refinement of the minimal gold model is the highest priority for future work. With this model, static and dynamic measurements can be combined in a meaningful way; without it, every sensor configuration requires its own calibration. Key decisions about the model—including the maximum number of parameters and realistic temperature/pressure derivatives—will need to be made. For example, it evident in Figure 4.2 that an second interband contribution begins at 3.5 eV, which would require three additional model parameters (weight, edge location, and broadening). Although this edge is outside of the spectral range accessible in dynamic measurements, the low energy tail might contribute to optimizations over visible wavelengths. Is this additional complexity worthwhile in a "minimal" model, or does it simply lead to von Neumann's jest[55]?

> "...with four parameters I can fit an elephant, and with five I can make him wiggle his trunk!"

Although eight parameters (four complex numbers) appear to be necessary for an elephant with a flexible trunk,[56] overfitting the problem is a valid concern. At the same time, the addition of a second interband transition might bring the ϵ_∞ closer to unity, at which point the parameter could be considered fixed (bringing the total number of parameters to eight). Common interband broadening values, or perhaps broadening derivatives, could be considered. Free and bound electron broadening seem to have similar logarithmic derivatives, so the number of free parameters may not further restricted. Since ambient model parameters can be determined from ellipsometry, it is really the number of significant parameter derivatives (not the number of optical parameters) that are important to gold sensor analysis. Some parameter variations, such as E_P, do not appear to strongly affect reflectance ratio calculations, so perhaps some of the derivatives can be ignored entirely. Parameter sensitivity studies and computational simulations of gold's optical properties would be extremely helpful. The optical model might also be tied to the equation of state for gold[57,58] to man-

age conversions between pressure and density. Final adjustments to the model parameters should be made with reliable dynamic measurements.

It is premature at this point to optimize the gold model with existing dynamic data. Improvements to the measurement are needed to complete gold sensor calibration and allow the sensors to be used in Z experiments. The most significant change that should be considered is the use an extended Lambertian source, which would to eliminate alignment/tilt issues. LaLone[59] describes an integrating sphere technique for dynamic reflectance measurements, which could be readily be applied to gold sensor studies. Upgrades to the streaked spectroscopy system are also necessary. Source reproducibility has been a recurring problem throughout this project, so simultaneous sample and reference measurements are strongly recommended. This added diagnostic burden, along with the eventual desire to field multiple gold sensors at the same time, poses serious economic challenges. If streak cameras continue to be used in gold sensor measurements, methods for recording multiple spectra on a camera will need to be developed. Alternative recording methods, such as the new LDRD project "Wavelength Conversion Arrays for Optical and X-Ray Diagnostics at Z", may play an important role in this area.

Thermal diffusion, mentioned only briefly in this report, will be a recurring topic in gold sensor applications. Careful reflectance measurements and a trustworthy optical model may reveal the temperature of a gold sensor, but the important task will be how to link this value to the actual temperature of interest. When the sample is in intimate contact with the sensor, the problem seems straightforward—the measurement probes the sample-window interface temperature—although thermal diffusivities are generally unknown at elevated pressures and temperatures. There may be a path forward, however, by driving samples onto gold sensors deposited onto different optical windows (sapphire, cubic zirconia, etc.). With the correct impact velocity, samples can be brought to the same pressure-temperature state while the interface temperature may be quite different. Comparing these measurements with the ambient window diffusivity, it should be possible to estimate the actual sample temperature and gain insight about sample diffusivity.

In this project, gold sensors were deposited onto the optical window, not the sample of interest. This approach works for Hugoniot temperature measurements (where the sample is placed on the projectile) and liquid cell measurements (where the rear window of the cell is gold coated), but most dynamic compression experiments are not performed in either configuration. Instead, a solid sample is usually bonded to an optical window and subjected to a dynamic load. If the gold sensor were deposited onto the window, the glue/epoxy layer would act as a thermal barrier, preventing the sensor from equilibrating with the sample. One solution to this problem would be to eliminate the glue bond via an ultrathin metal bond.

sample–adhesion layer–gold coating↔gold sensor–window

This may work but has not yet been tested for dynamic compression samples/windows. Another possible solution would be to place the sensor directly on the the sample, measuring

reflectance through the window and transparent bond layer.

sample–adhesion layer–gold sensor↔bond layer↔window

This approach places the sensor in direct contact with the sample and can make use of an adhesion layer, but there are several potential problems. The bond layer must remain optically transparent during the experiment, and its dynamic refractive index would need to be known for data reduction. Thin bond layers, which are usually desirable, may complicate the analysis by acting as an optical etalon. Liquid windows, such as zinc chloride[60] or liquid xenon,[61] avoid the etalon problem but may create other challenges; a liquid bonding layer, such as hexane might be a useful compromise. Interface issues are a recurring problem in dynamic temperature measurements[62,63] and will continue to be an issue with gold sensors.

This page intentionally left blank.

References

[1] D.B. Reisman, A. Toor, R.C. Cauble, C.A. Hall, J.R. Asay, M.D. Knudsen, M.D. and M.D. Furnish. Magnetically driven isentropic compression experiments on the z accelerator. *Journal of Applied Physics* **89**, 1625 (2001).

[2] H.B. Callen. *Thermodynamics and an Introduction to Statistical Mechanics.* Wiley, New York, 2nd edition, (1985).

[3] G.E. Duvall and R.A. Graham. Phase transitions under shock wave loading. *Reviews of Modern Physics* **49**(3), 523 (1977).

[4] J.M Winey, G.E. Duvall, M.D. Knudson, and Y.M. Gupta. Equation of state and temperature measurements for shocked nitromethane. *Journal of Chemical Physics* **113**(17), 7492 (2000).

[5] D.D. Bloomquist and S.A. Sheffield. Thermocouple temperature measurements in shock-compressed solids. *Journal of Applied Physics* **51**(10), 5260 (1980).

[6] D.D. Bloomquist and S.A. Sheffield. Shock-compression temperature rise in polymethyl methacrylate determined from resistivity of embedded copper foils. *Applied Physics Letters* **38**(3), 185 (1981).

[7] G.A. Lyzenga, T.J. Ahrens, W.J Nellis, and A.C. Mitchell. The temperature of shock-compressed water. *Journal of Chemical Physics* **76**(12), 6282 (1982).

[8] D. Partouche-Sebban, J.L. Pelissier, F.G. Abeyta, W.W. Anderson, M.E. Byers, D. Dennis-Koller, J.S. Esparza, R.S. Hixson, D.B. Holtkamp, B.J. Jensen, J.C. King, P.A. Rigg, P. Rodriguez, D.L. Shampine, J.B. Stone, D.T. Westley, S.D. Borror,and C.A. Kruschwitz. Measurement of the shock-heated melt curve of lead using pyrometry and reflectometry. *Journal of Applied Physics* **97**, 43521 (2005).

[9] T.A. Friedmann, J.-P. Davis, R.E. Setchell, M.U. Anderson, M.D. Knudson, T.J. Vogler, and C.S. Alexander. Embedded sensors for dynamic compression experiments. Technical Report SAND2007-0485, Sandia National Laboratories, (2007).

[10] V.W. Yuan, J.D. Bowman, D.J. Funk, G.L. Morgan, R.L. Rabie, C.E. Ragan, J.P. Quintana,and H.L. Stacy. Shock temperature measurement using neutron resonance spectroscopy. *Physical Review Letters* **94**, 125504 (2005).

[11] G. Tessier, S. Hole, and D. Fournier. Quantitative thermal imaging by synchronous thermoreflectance with optimized illumination wavelengths. *Applied Physics Letters* **78**, 2267 (2001).

[12] G. Tessier, G. Jerosolimski, S. Hole, D. Fournier, and C. Filloy. Measuring and predicting the thermoreflectance sensitivity as a function of wavelength on encapsulated materials. *Review of Scientific Instruments* **74**, 495 (2003).

[13] M. Farzaneh, K. Maize, D. Lüerben, J.A. Summers, P.M. Mayer, P.E. Raad, K.P. Pipe, A. Shakouri, R.J. Ram, and J.A Hudgings. CCD-based thermoreflectance microscopy: principles and applications. *Journal of Physics D* **42**, 143001 (2009).

[14] Y. Wang, J.Y. Park, Y.K. Koh, and D.G. Cahill. Thermoreflectance of metal transducers for time-domain thermoreflectance. *Journal of Applied Physics* **108**, 043507 (2010).

[15] A. Beran. The reflectance behaviour of gold at temperatures up to 500° C. *Tschemaks Min. Petr. Mitt.* **34**, 211 (1985).

[16] R. Weil. The variation with temperature of metallic reflectivity. *Proceedings of the Physical Society* **60**, 8 (1948).

[17] O.T. Strand, D.R. Goosman, C. Martinez, T.L. Whitworth, and W.W. Kuhlow. Compact system for high-speed velocimetry using heterodyne techniques. *Review of Scientific Instruments* **77**, 83108 (2006).

[18] L.G. Schulz. The optical constants of silver, gold, copper, and aluminium. I. The absorption coefficient k. *Journal of the Optical Society of America* **44**, 357 (1954).

[19] L.G. Schulz. The optical constants of silver, gold, copper, and aluminium. II. The index of refraction n. *Journal of the Optical Society of America* **44**, 362 (1954).

[20] M. Otter. Optishe konstanten massiver metalle. *Zeitschrift fur Physik* **161**, 163 (1961).

[21] R.H. Doremus. Reflectivity of silver and gold. *Journal of Applied Physics* **36**, 2853 (1965).

[22] M. Theye. Investigation of the optical properties of Au by means of thin semitransparent samples. *Physical Review B* **2**, 3060 (1970).

[23] P.B. Johnson and R.W. Christy. Optical constants of the noble metals. *Physical Review B* **6**, 4370 (1972).

[24] O. Loebich. The optical properties of gold. *Gold Bulletin* **5**(1), 2 (1972).

[25] E.D. Palik, editor. *Handbook of Optical Constants of Solids.* Academic Press, (1985).

[26] A.G. Worthing. Spectral emissivitires of tantalum, platinum, nickel, and gold as function of temperature and the melting point of tantalum. *Physical Review* **28**, 174 (1926).

[27] U. Schley, C. Tingwaldt, and J. Verch. Thermooptische eigensehaften yon gold und platin. *Naturewissenschaften* **47**, 222 (1960).

[28] M. Otter. Temperaturabh angigkeit der optischen Konstanten massiver Metalle. *Zeitschrift fur Physik* **161**, 539 (1961).

[29] H. Watanabe, M. Susa, H. Fukuyama, and K. Nagata. Phase dependence (liquid/solid) of normal spectral emissivities of noble metals at melting points. *International Journal of Thermophysics* **24**, 223 (2003).

[30] T. Hollstein, U. Kreibin, and F. Leis. Optical Properties of Au and A1 in the Visible, Determined at 300and 1.5 K. *Physica Status Solidi (b)* **83**, K49 (1977).

[31] D. Errandonea. The melting curve of ten metals up to 12 GPa and 1600 K. *Journal of Applied Physics* **108**, 033517 (2010).

[32] J.E. Davey and T. Pankey. Optical properties of cold- and hot-deposited gold films. *Journal of Applied Physics* **36**, 2571 (1965).

[33] D.E. Aspnes, E. Kinsbron, and D.D. Bacon. Optical properties of Au: sample effects. *Physical Review B* **21**, 3290 (1980).

[34] M.J. Rost, D.A. Quist, and J.W.M. Frenken. Grains, growth, and grooving. *Physical Review Letters* **91**, 26101 (2003).

[35] V.R. Romanyuk, O.S. Kondratenko, O.V. Fursenko, O.S. Lytvyn, S.A. Zynyo, and A.A. Korhcovyi and N.L. Dmitruk. Thermally induced changes in thin gold films detected by polaritonic ellipsometry. *Materials Science and Engineering B* **149**, 285 (2008).

[36] H. Okamoto and T.B. Massalski. The Au-Pt (gold-platinum) system. *Bulletin of Alloy Phase Diagrams* **6**, 46 (1985).

[37] C.T. Seagle and D.H. Dolan. Visible reflectivity system for high-pressure studies. *Review of Scientific Instruments* **84**, 066104 (2013).

[38] G.J. Piermarini, S. Block, and J.D. Barnett. Hydrostatic limits in liquids and solids to 100 kbar. *Journal of Applied Physics* **44**, 5377 (1973).

[39] S.C. Jones and Y.M. Gupta. Refractive index and elastic properties of z-cut quartz shocked to 60 kbar. *Journal of Applied Physics* **88**, 5671 (2000).

[40] H.S. Carslaw and J.C. Jaeger. *Conduction of heat in solids*. Oxford University Press, Oxford, 2nd edition, (1959).

[41] M. Dressel and G. Grüner. *Electrodynamics of solids: optical properties of electrons in matter*. Cambridge University Press, (2002).

[42] A. Vial, A. Grimault, D. Macias, D. Barchiese, and M.L. de la Chappelle. Improved analytical fit of gold dispersion: application to the modeling of extinction spectra with a finite-difference time-domain method. *Physical Review B* **71**, 85416 (2005).

[43] F. Hao and P. Nordlander. Efficient dielectric function for FDTD simulation of the optical properties of silver and gold nanoparticles. *Chemical Physics Letters* **446**, 115 (2007).

[44] P.G. Etchegoin, E.C. Le Ru, and M. Meyer. An analytic model for the optical properties of gold. *Journal of Chemical Physics* **125**, 164705 (2006).

[45] P.E. Hopkins. Influence of electron-boundary scattering on thermoreflectance calculations after intra- and interband transitions induced by a a short-pulsed laser. *Physical Review B* **81**, 35413 (2010).

[46] A.D. Rakic, A.B. Djurisic, J.M. Elazar, and M.L. Majewski. Optical properties of metallic films for vertical-cavity optoelectronic devices. *Applied Optics* **37**, 5271 (1998).

[47] R. Brendel and D. Bormann. An infrared dielectric function model for amorphous solids. *Journal of Applied Physics* **71**, 1 (1992).

[48] M.A. Ordal, R.J. Bell, R.W. Alexander, L.L. Long, and M.R. Querry. Optical properties of fourteen metals in the infrared and far infrared: Al, Co, Cu, Au, Fe, Pb, Mo, Ni, Pd, Pt, Ag, Ti, V, and W. *Applied Optics* **24**, 4493 (1985).

[49] A. Moroz. Drude model parameters to fit the dielectric function of free electron metals including plasma frequencies and damping constants for Ag, Al, Au, Cu, K, Na, Pt, `http://www.wave-scattering.com/drudefit.html`, (2011).

[50] D.L. Decker and H.B. Vanfleet. Melting and high-temperature electrical resistance of gold under pressure. *Physical Review* **138**, A129 (1965).

[51] P. Winemius, F.F. van Kampen, H.P. Lengkeek, and C.G. van Went. Temperature dependence of the optical properties of Au, Ag, and Cu. *Journal of Physics F* **6**, 1583 (1976).

[52] F. Peter. Über Brechungsindizes und Absorptionskonstanten des Diamanten zwischen 644 und 226 mμ. *Zeitschrift für Physik* **15**, 358 (1923).

[53] A.C. DeFranzo and B.G. Pazol. Index of refraction measurement on sapphire at low temperatuers and visible wavelengths. *Applied Optics* **32**(13), 2224 (1993).

[54] C. Moler. *Numerical Computing with MATLAB*. Society for Industrial and Applied Mathematics, (2004).

[55] F. Dyson. A meeting with Enrico Fermi. *Nature* **427**, 297 (2004).

[56] J. Mayer, K. Khairy, and J. Howard. Drawing an elephant with four complex parameters. *American Journal of Physics* **78**, 648 (2010).

[57] S.H. Shim, T.S. Duffy, and T. Kenichi. Equation of state of gold and its applications to the phase boundaries near 660 km depth in Earth's mantle. *Earth and Planetary Science Letters* **203**, 729 (2002).

[58] Y. Fei, J. Li, K. Hirose, W. Minarik, J. Van Orman, C. Sanloup, W. van Westrenen, T. Komabayushi, and K. Fukuoka. A critical evaluation of pressure scales at high temperatures by in situ x-ray diffraction experiments. *Physics of Earth and Planetary Interiors* **143–144**, 515 (2004).

[59] B.M LaLone, G.D. Stevens, W.D. Turley, D.B. Holtkamp, A.J. Iverson, R.S. Hixson, and L.R. Veeser. Release path temperatures of shock-compressed tin from dynamic reflectance and radiance measurements. *Journal of Applied Physics* **114**, 063506 (2013).

[60] J.L. Wise. Refractive index and equation of state of a shock-compressed aqueous solution of zinc chloride. In *Shock Waves in Condensed Matter,* Asay, J., editor, 317 (Elsevier, Santa Fe, NM, 1983).

[61] S. Root, R.J. Magyar, J.H. Carpenter, D.L. Hanson, and T.R. Mattsson. Shock compression of a fifth period element: liquid xenon to 840 GPa. *Physical Review Letters* **105**, 085501 (2010).

[62] P.A. Urtiew and R. Grover. Temperature deposition caused by shock interactions with material interfaces. *Journal of Applied Physics* **45**(1), 140 (1974).

[63] R. Grover and P.A. Urtiew. Thermal relaxation at interfaces following shock compression. *Journal of Applied Physics* **45**(1), 146 (1974).

DISTRIBUTION:

3 National Security Technologies
Los Alamos Operations
P.O. Box 809
Los Alamos, NM 87544
Attn: D. Esquibel
R. Hixson
A. Iverson

2 National Security Technologies
Las Vegas Operations
PO Box 98521
Las Vegas, NV 89193
Attn: S.A. Becker
S. Goldstein

3 National Security Technologies
Special Technologies Laboratory
5520 "B" Ekwill Street
Santa Barbara, CA 93111
Attn: B. Lalone
G. Stevens
W.D. Turley

6 Los Alamos National Laboratory
P.O. Box 1663
Los Alamos, NM 87545
Attn: C. Bolme
R.L. Gustavsen
D. Holtkamp
B.J. Jensen
S. Sheffield
N. Velisavljevic

1 MS 0155 C.A. Hall, 6601
1 MS 0346 L.M. Phinney, 1512
1 MS 0425 S.C. Jones, 245
1 MS 0959 J.A. Romero, 1832
1 MS 0959 C.E. Sobczak, 1832
1 MS 1085 E.J. Skogen, 1742
1 MS 1106 T. Ao, 1646
1 MS 1106 A. Shay, 1342
1 MS 1189 J.-P. Davis, 1646
1 MS 1189 M.P Desjarlais, 1600
1 MS 1189 D.H. Dolan, 1646
1 MS 1189 T. Mattsson, 1641

1	MS 1189	S. Root, 1646
1	MS 1189	L. Shulenburger, 1641
1	MS 1189	C.T. Seagle, 1646
1	MS 1190	D. Bliss, 1675
1	MS 1190	G. Rochau, 1675
1	MS 1193	M. Gomez, 1683
1	MS 1193	R.G. Hacking, 16561
1	MS 1193	A. Lewis, 16561
1	MS 1193	C. Smith, 16561
1	MS 1195	S.C. Alexander, 1646
1	MS 1195	J.R. Asay, 1646
1	MS 1195	J. Brown, 1646
1	MS 1195	D. Dalton, 1646
1	MS 1195	D. Flicker, 1640
1	MS 1195	M.D. Furnish, 1646
1	MS 1195	R.J. Hickman, 1647
1	MS 1195	M.D. Knudson, 1646
1	MS 1195	G.T. Leifeste, 1647
1	MS 1195	W.D. Reinhart, 1647
1	MS 1195	J. Wise, 1646
1	MS 1349	H. Fan, 1815
1	MS 1454	B.A. Jilek, 2554
1	MS 9042	T.J. Vogler, 8256
1	MS 0899	Technical Library, 9536 (electronic copy)
1	MS 0359	D. Chavez, LDRD Office, 1911

This page intentionally left blank.

Sandia National Laboratories